

Contents

Thermal and non-thermal emission from circumstellar interaction	3
Roger A. Chevalier and Claes Fransson	
1 Introduction	3
2 Initial conditions	4
2.1 Ejecta structure	4
2.2 Ambient medium	5
3 Shock interaction	7
3.1 Shock structure and evolution	7
3.2 Postshock conditions and radiative cooling	8
3.3 Asymmetries, shells and clumping	13
4 Thermal emission from hot gas	14
4.1 Optically thin emission	14
4.2 Optically thick emission	16
4.3 Reprocessing of X-rays	17
5 Non-thermal emission from relativistic particles	19
5.1 Particle acceleration and magnetic field amplification in shocks	19
5.2 Optically thin synchrotron emission	23
5.3 Inverse Compton X-ray emission	24
5.4 The radio spectrum including absorption processes	26
5.5 Radio and high energy signatures of cosmic ray acceleration	31
6 Examples of circumstellar emission from different SN types	32
6.1 Type IIP	32
6.2 Type III	34
6.3 Type IIb	35
6.4 Type IIn	39
6.5 SN 1987A	42
6.6 Type Ib/c	47
6.7 Type Ibn	49
6.8 Relativistic expanding supernovae	50

6.9	Type Ia	50
7	Conclusions	52
	References	53

Thermal and non-thermal emission from circumstellar interaction

Roger A. Chevalier and Claes Fransson

Abstract It has become clear during the last decades that the interaction between the supernova ejecta and the circumstellar medium is playing a major role both for the observational properties of the supernova and for understanding the evolution of the progenitor star leading up to the explosion. In addition, it provides an opportunity to understand the shock physics connected to both thermal and non-thermal processes, including relativistic particle acceleration, radiation processes and the hydrodynamics of shock waves. This chapter has an emphasis on the information we can get from radio and X-ray observations, but also their connection to observations in the optical and ultraviolet. We first review the different physical processes involved in circumstellar interaction, including hydrodynamics, thermal X-ray emission, acceleration of relativistic particles and non-emission processes in the radio and X-ray ranges. Finally, we discuss applications of these to different types of supernovae.

1 Introduction

This review is partly an update of our previous review from 2003 on circumstellar interaction [39], mainly adding new developments during the last decade. In this review we are mainly concentrating on the physical processes, and only discuss individual objects of different supernova types as examples of these. While the focus is on radio and X-rays there is an especially close connection between the X-rays and optical observations, and where relevant we also discuss observations in this wavelength band.

Roger A. Chevalier
Dept. of Astronomy, University of Virginia, P.O. Box 400325 Charlottesville, VA 22904, USA,
e-mail: rac5x@virginia.edu

Claes Fransson
Stockholm University, Department of Astronomy and Oskar Klein Centre, AlbaNova, S - 106 91
Stockholm, Sweden, e-mail: claes@astro.su.se

Massive stars are known to have strong winds during their lives. At the time of the supernova (SN hereafter) explosion, the rapidly expanding gas plows into the surrounding medium, creating shock waves. The shock waves heat the gas, giving rise to X-ray emission. A fraction of this may be reprocessed into optical and ultraviolet (UV) radiation, which in extreme cases may dominate the emission from the SN ejecta. The shock waves also accelerate particles to relativistic speeds. Relativistic electrons radiate synchrotron emission in the magnetic fields that are present; the magnetic field may be amplified by turbulence near the shock and/or the downstream region.

2 Initial conditions

For the most part, the structure of the supernova ejecta can be separated from that of the ambient medium and then their interaction can be discussed. This is not the case around the time of shock breakout, when the diffusion time for photons in the shocked region first becomes comparable to the age of the supernova. Radiative acceleration of the pre-shock gas leads to the dissolution of the radiation dominated shock wave, which is followed by the formation of a viscous shock wave in the surrounding medium. Radiative pre-acceleration of surrounding gas gives a velocity $v \propto r^{-2}$ due to the flux divergence and is typically only important at early times.

2.1 Ejecta structure

After the shock wave has passed through the progenitor star, the gas evolves to free expansion, $v = r/t$ where t is the age of the explosion. In free expansion, the density of an element of gas drops as t^{-3} so that the density profile is described by a function $\propto t^{-3} f(r/t)$.

The profile $f(r/t)$ can typically be described by a function that is a steep power law at high velocities and flat in the central region. The outer steep power law region is especially important for circumstellar interaction because it is the region that typically gives rise to the observed emission. The outer edge of a star has a density profile that can be approximated by $\rho = a(r_* - r)^\delta$, where a is a constant and r_* is the outer edge of the star. For a radiative envelope, $\delta = 3$ and for a convective envelope, $\delta \approx 1.5$.

The supernova shock wave accelerates through the outer layers of the star due to the cumulation effect of energy going into a vanishingly small amount of matter. The acceleration of the shock wave through the outer layers of the star and the subsequent evolution to free expansion can be described by a self-similar solution [133]. The power law exponent in this case is not determined by dimensional analysis, but by the passing of the solution through a critical point; it is a self-similar solution of the second kind. The solution applies to a planar shock breakout, i.e. the

breakout occurs over a distance that is small compared to stellar radius. In that case the power law profile is steepened by two powers of r in going to spherical expansion. The result of the self-similar solution is that $n = 10.2$ for $\delta = 3$ and $n = 12$ for $\delta = 1.5$. There is also a self-similar solution for an accelerating shock in an atmosphere with an exponential density profile. The resulting value of n is 8.67, which is also the value obtained in the limit $\delta \rightarrow \infty$.

The overall result of these considerations is that the outer part of a core collapse supernova can be approximated by a steep power law density profile, or $\rho_{\text{ej}} \propto r^{-n}$ where n is a constant. After the first few days the outer parts of the ejecta expand with constant velocity, $V(m) \propto r$ for each mass element, m , so that $r(m) = V(m)t$ and $\rho(m) = \rho_o(m)(t_o/t)^3$. Therefore

$$\rho_{\text{ej}} = \rho_o \left(\frac{t}{t_o} \right)^{-3} \left(\frac{V_o t}{r} \right)^n. \quad (1)$$

This expression takes into account the free expansion of the gas.

The inner density distribution cannot be analytically calculated in a straightforward way, but physical arguments imply a roughly r^{-1} density profile [44, 106]. Although the outer power law density index is found from the self-similar solution, the coefficient of the density must be determined by numerical simulation of the whole explosion. The outer power law is only approached asymptotically so the power law index of the density profile applicable to a given situation is smaller than the asymptotic value.

The self-similar solution assumes that the flow is adiabatic, which is not the case once radiation can diffuse from the shocked layer. For a radiation dominated shock, the shock thickness corresponds to an optical depth of approximately $\tau_s = c/v$, where v is the shock velocity and c is the speed of light. Once the shock wave reaches an optical depth of τ_s from the surface, radiation can escape and the shock wave acceleration through the layers of decreasing density ends.

2.2 Ambient medium

Because of their large luminosity massive stars lose mass in all evolutionary stages. What is most important for at least the early interaction between the supernova and ambient medium is the mass loss immediately before the explosion. Red supergiants have slow winds with velocities $10 - 50 \text{ km s}^{-1}$. The mass loss rates of most red supergiants are in the range $10^{-6} - 10^{-5} M_{\odot} \text{ yr}^{-1}$, but there are also a number of stars undergoing a super-wind phase with very high mass loss rate, $10^{-4} - 10^{-3} M_{\odot} \text{ yr}^{-1}$. This includes stars like VY CMa, NML Cyg and IRC10420. It is obvious both from the mass loss rates and their small fraction of the total number of red supergiants that this is a short-lived phase. Compact progenitors, like WR-stars and blue supergiants, have similar mass loss rates $10^{-6} - 10^{-4} M_{\odot} \text{ yr}^{-1}$ but wind velocities $1000 - 3000 \text{ km s}^{-1}$. See [137] for an extended discussion.

There are supernovae that show evidence for larger mass loss rates occurring somewhat before the supernova explosion, in particular Type II_n SNe (see Sect. 6.4 and [138]). The driving mechanism for the mass loss is not understood, nor is the reason why it should occur close to the time of the explosion. Such strong mass loss rates are observed during the outbursts of Luminous Blue Variables (LBVs) and they are frequently mentioned in this context. Other possibilities are turbulence in the late phases of stellar evolution and/or binary interaction [34, 134, 138].

If the mass loss parameters stay approximately constant leading up to the explosion, the circumstellar density is given by

$$\rho_{\text{cs}} = \frac{\dot{M}}{4\pi u_w r^2}. \quad (2)$$

In most cases it is the CSM density which is most observationally relevant and can be measured. It is therefore convenient to scale this by the mass loss rate and wind velocity to that typical of a red supergiant. We therefore introduce a mass loss rate parameter C_* defined by

$$\frac{\dot{M}}{u_w} = 6.303 \times 10^{14} \left(\frac{\dot{M}}{10^{-5} M_\odot \text{ yr}^{-1}} \right) \left(\frac{u_w}{10 \text{ km s}^{-1}} \right)^{-1} \equiv 6.303 \times 10^{14} C_* \text{ g cm}^{-1} \quad (3)$$

The CS density is then

$$\rho_{\text{cs}} = 5.016 \times 10^{-17} C_* \left(\frac{r}{10^{15} \text{ cm}} \right)^{-2} \text{ g cm}^{-3}. \quad (4)$$

Note that C_* varies by a large factor for different types of progenitors. For a red supergiant with $\dot{M} = 10^{-5} M_\odot \text{ yr}^{-1}$ and $u_w \approx 10 \text{ km s}^{-1}$ $C_* \sim 1$, while for a fast wind, like that from a WR star or blue supergiant with $u_w \approx 1000 \text{ km s}^{-1}$, $C_* \sim 0.01$ for the same mass loss rate. An LBV with $\dot{M} = 0.1 M_\odot \text{ yr}^{-1}$ and $u_w \approx 100 \text{ km s}^{-1}$ has $C_* \sim 10^3$.

Most of our discussion in the following will be based on the assumption of a spherical geometry. There is, however, strong evidence that both the ejecta and the CSM may be very complex. An example of a both anisotropic and clumpy CSM medium is that of the red supergiant VY CMa [140], while the famous Eta Car nebula has a more regular, bipolar structure, with a dense shell containing $\sim 10 M_\odot$ of mainly molecular gas [136]. Both anisotropies and clumpiness can have strong observational consequences for the CSM interaction with the SN ejecta.

3 Shock interaction

3.1 Shock structure and evolution

When the radiation dominated shock front in a supernova nears the stellar surface, a radiative precursor to the shock forms when the radiative diffusion time is comparable to the propagation time. There is radiative acceleration of the gas and the shock disappears when optical depth $\sim c/\nu$ is reached [59]. The fact that the velocity decreases with radius implies that the shock will re-form as a viscous shock in the circumstellar wind. This occurs when the supernova has approximately doubled in radius.

The interaction of the ejecta, expanding with velocity $\gtrsim 10^4$ km s $^{-1}$, and the nearly stationary circumstellar medium results in a reverse shock wave propagating inwards (in mass), and an outgoing circumstellar shock. The density in the circumstellar gas is given by Eq. (2). As discussed above, hydrodynamical calculations show that to a good approximation the ejecta density can be described by Eq. (1). A useful self-similar solution for the interaction can then be found [28, 29, 114]. Here we sketch a simple derivation. More details can be found in these papers, as well as in the review [31].

Assume that the shocked gas can be treated as a thin shell with mass M_s , velocity V_s , and radius R_s . Balancing the ram pressure from the circumstellar gas and the impacting ejecta, the momentum equation for the shocked shell of circumstellar gas and ejecta is

$$M_s \frac{dV_s}{dt} = 4\pi R_s^2 [\rho_{ej}(V_{ej} - V_s)^2 - \rho_{cs} V_s^2]. \quad (5)$$

Here, M_s is the sum of the mass of the shocked ejecta and circumstellar gas. The swept up mass behind the circumstellar shock is $M_{cs} = \dot{M} R_s / u_w$, and that behind the reverse shock $M_{rev} = 4\pi \int_{R_s}^{\infty} \rho(r) r^2 dr = 4\pi t_o^3 V_o^n (t/R_s)^{n-3} / (n-3)$, assuming that $R_s \gg R_p$, the radius of the progenitor. With $V_{ej} = R_s/t$ we obtain

$$\left[\frac{\dot{M}}{u_w} R_s + \frac{4\pi \rho_o t_o^3 V_o^n t^{n-3}}{(n-3) R_s^{n-3}} \right] \frac{d^2 R_s}{dt^2} = 4\pi R_s^2 \left[\frac{\rho_o t_o^3 V_o^n t^{n-3}}{R_s^n} \left(\frac{R_s}{t} - \frac{dR_s}{dt} \right)^2 - \frac{\dot{M}}{4\pi u_w R_s^2} \left(\frac{dR_s}{dt} \right)^2 \right]. \quad (6)$$

This equation has the power law solution

$$R_s(t) = \left[\frac{8\pi \rho_o t_o^3 V_o^n u_w}{(n-4)(n-3) \dot{M}} \right]^{1/(n-2)} t^{(n-3)/(n-2)}. \quad (7)$$

The form of this similarity solution can be written down directly by dimensional analysis from the only two independent quantities available, $\rho_o t_o^3 V_o^n$ and \dot{M}/u_w . The solution applies after a few expansion times, when the initial radius has been

‘forgotten.’ The requirement of a finite energy in the flow implies $n > 5$. More accurate similarity solutions, taking the structure within the shell into account, are given in [28, 114]. In general, these solutions differ by less than $\sim 30\%$ from the thin shell approximation.

3.2 Postshock conditions and radiative cooling

The maximum ejecta velocity close to the reverse shock depends on time as $V_{\text{ej}} = R_s/t \propto t^{-1/(n-2)}$. The velocity of the circumstellar shock is

$$V_s(t) = \frac{dR_s(t)}{dt} = \frac{(n-3)R_s(t)}{(n-2)t} = \frac{(n-3)}{(n-2)}V_{\text{ej}} \propto t^{-1/(n-2)}. \quad (8)$$

with $R_s(t)$ given by Eq. (7), while the reverse shock velocity is

$$V_{\text{rev}} = V_{\text{ej}} - V_s = \frac{V_{\text{ej}}}{(n-2)}. \quad (9)$$

Assuming cosmic abundances and equipartition between ions and electrons, the temperature of the shocked circumstellar gas is

$$T_{\text{cs}} = 1.36 \times 10^9 \left(\frac{n-3}{n-2} \right)^2 \left(\frac{V_{\text{ej}}}{10^4 \text{ km s}^{-1}} \right)^2 \text{ K} \quad (10)$$

and at the reverse shock

$$T_{\text{rev}} = \frac{T_{\text{cs}}}{(n-3)^2}. \quad (11)$$

The time scale for equipartition between electrons and ions is

$$t_{\text{eq}} \approx 2.5 \times 10^7 \left(\frac{T_e}{10^9 \text{ K}} \right)^{1.5} \left(\frac{n_e}{10^7 \text{ cm}^{-3}} \right)^{-1} \text{ s}. \quad (12)$$

One finds that the reverse shock is marginally in equipartition, unless the temperature is $\gtrsim 5 \times 10^8$ K. The ion temperature behind the circumstellar shock is $\gtrsim 6 \times 10^9$ K for $V_4 \gtrsim 1.5$, and the density a factor $\gtrsim 4$ lower than behind the reverse shock. Ion-electron collisions are therefore ineffective, and $T_e \ll T_{\text{ion}}$, unless efficient plasma instabilities heat the electrons collisionlessly (Fig. 1).

For typical parameters, the electron temperatures of the two shocks are very different, $\sim (1-3) \times 10^9$ K for the circumstellar shock and $10^7 - 5 \times 10^8$ K for the reverse shock, depending on n . The radiation from the reverse shock is mainly below ~ 20 keV, while that from the circumstellar shock is above ~ 50 keV.

With $\rho_{\text{rev}}/\rho_{\text{cs}} = \rho_{\text{ej}}/\rho_{\text{wind}} = 4\pi u_w \rho_o t_o^3 V_o^n t^{n-3} / (MR^{n-2})$ one gets for the density behind the reverse shock

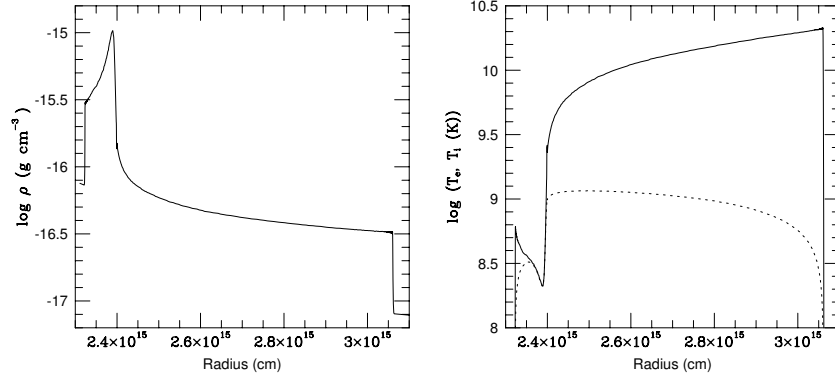


Fig. 1 Density and temperature structure of the reverse and circumstellar shocks for $n = 7$ and a velocity of $2.5 \times 10^4 \text{ km s}^{-1}$ at 10 days. Both shocks are assumed to be adiabatic. Because of the slow Coulomb equipartition the electron temperature (dotted line) is much lower than the ion temperature (solid line) behind the circumstellar shock.

$$\rho_{\text{rev}} = \frac{(n-4)(n-3)}{2} \rho_{\text{cs}}. \quad (13)$$

Therefore the density behind the reverse shock is much higher than behind the circumstellar shock for $n \gtrsim 7$. There is a drop in density across the contact discontinuity, moving from the shocked ejecta to the circumstellar medium (see Fig. 1).

The fact that low density gas is decelerating higher density gas leads to a Rayleigh-Taylor instability. Chevalier, Blondin & Emmering [35] have calculated the structure using a two-dimensional PPM (piecewise parabolic method) hydrodynamic code. They indeed find that instabilities develop, with dense, shocked ejecta gas penetrating into the hotter, low density shocked circumstellar gas (Fig. 2). The instability mainly distorts the contact surface, and does not seriously affect the general dynamics. The calculation assumed that cooling is not important. If the gas at the reverse shock cools efficiently, the extent of the instability is similar, although the Rayleigh-Taylor fingers are narrower [27].

The above expressions for the density and temperature apply to the gas immediately behind the reverse shock. However, radiative cooling may be important in many cases resulting in lower temperature, higher densities and higher luminosity of the gas. For $T_e \gtrsim 2.6 \times 10^7 \text{ K}$ free-free cooling dominates with a cooling rate $\Lambda \approx 1.0 \times 10^{-23} (T_e/10^7 \text{ K})^{0.5} \text{ erg s}^{-1} \text{ cm}^3$. Assuming isobaric cooling behind the shock, one obtains for the cooling time $t_{\text{cool}} = 5kT_e/n_H\Lambda(T_e)$

$$t_{\text{cool}} = \frac{13.5}{(n-2)(n-3)(n-4)} C_*^{-1} \left(\frac{V_{\text{ej}}}{10^4 \text{ km s}^{-1}} \right)^3 \left(\frac{t}{\text{days}} \right)^2 \text{ days}, \quad (14)$$

At $T_e \lesssim 2.6 \times 10^7 \text{ K}$, line emission increases the cooling rate and $\Lambda(T_e) \approx 2.4 \times 10^{-23} (T_e/10^7 \text{ K})^{-0.48} \text{ erg s}^{-1} \text{ cm}^3$ for solar abundances. The cooling time then

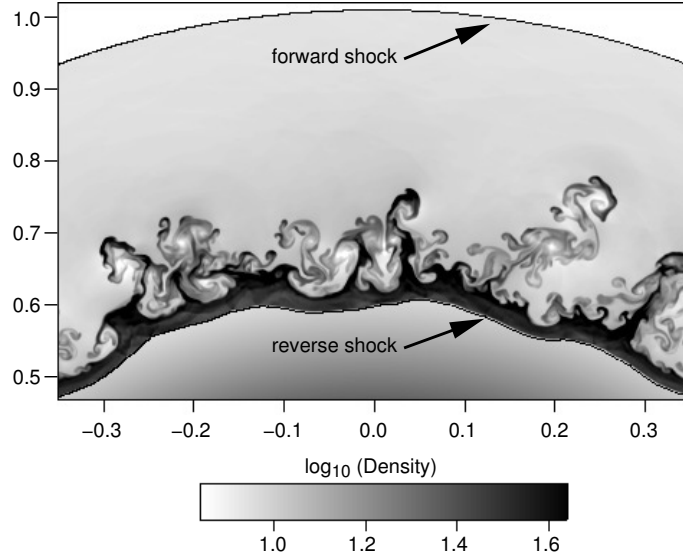


Fig. 2 Two-dimensional calculation of the shock structure for a supernova with $n = 6$ in a stellar wind. Cooling is not included here. (Courtesy John Blondin).

becomes

$$t_{\text{cool}} = \frac{1.0 \times 10^3}{(n-3)(n-4)(n-2)^{3.34}} C_*^{-1} \left(\frac{V_{\text{ej}}}{10^4 \text{ km s}^{-1}} \right)^{5.34} \left(\frac{t}{\text{days}} \right)^2 \text{ days}, \quad (15)$$

again assuming solar abundances [76]. From these expressions it is clear that the cooling time is very sensitive to the density gradient, as well as the shock velocity and mass loss rate. If the temperature of the reverse shock falls below $\sim 2 \times 10^7$ K, a thermal instability may occur and the gas cools to $\lesssim 10^4$ K, where photoelectric heating from the shocks balances the cooling [67, 37]. Because of its low temperature and high density this is usually referred as the cool, dense shell, and can have important observational consequences. In case the reverse shock has propagated into the processed material, as may occur comparatively early in Type IIb and Ib/c SNe, the cooling may be further enhanced due to the higher metallicity. The above expressions should then be modified as discussed in [120], resulting in a prolonged radiative phase for the reverse shock.

SNe with high mass loss rates, $C_* \gtrsim 5$, generally have radiative reverse shocks for $\gtrsim 100$ days, while SNe with lower mass loss rates, like the Type IIP SNe, have adiabatic shocks from early times.

If cooling, the total energy emitted from the reverse shock is [67]

$$L_{\text{rev}} = 4\pi R_s^2 \frac{1}{2} \rho_{\text{ej}} V_{\text{rev}}^3 = \frac{(n-3)(n-4)}{4(n-2)^3} \frac{\dot{M} V^3}{u_w}$$

$$= 1.6 \times 10^{41} \frac{(n-3)(n-4)}{(n-2)^3} C_* V_4^3 \text{ erg s}^{-1}. \quad (16)$$

Most of this is emitted as soft X-rays. Because of the large column density of the cool, dense shell most of this radiation will, however, be thermalized into UV and optical emission. For high \dot{M}/u_w the luminosity from the reverse shock may therefore contribute appreciably, or even dominate, the bolometric luminosity.

Because $V \propto t^{-1/(n-2)}$, $L_{\text{rev}} \propto t^{-3/(n-2)}$ in the cooling case. However, one of the most important effects of the cooling is that the cool gas may absorb most of the emission from the reverse shock. Therefore, in spite of the higher intrinsic luminosity of the reverse shock, little of this will be directly observable. The column density of the cool gas is given by $N_{\text{cool}} = M_{\text{rev}}/(4\pi R_s^2 m_p)$, or

$$N_{\text{cool}} \approx 1.0 \times 10^{21} (n-4) C_* \left(\frac{V_{\text{ej}}}{10^4 \text{ km s}^{-1}} \right)^{-1} \left(\frac{t}{100 \text{ days}} \right)^{-1} \text{ cm}^{-2}. \quad (17)$$

Because the threshold energy due to photoelectric absorption is related to N_{cool} by $E(\tau = 1) = 1.2(N_{\text{cool}}/10^{22} \text{ cm}^{-2})^{3/8} \text{ keV}$, it is clear that the emission from the reverse shock is strongly affected by the cool shell, and a transition from optically thick to optically thin is expected during the first months, or year. Examples of this are discussed in connection to SN 1993J in Sect. 6.3 and SN 2010jl in Sect. 6.4.

Because of the high density in combination with low temperature the cool, dense shell may also be a site of dust formation. This, however, requires a temperature of $\lesssim 2000 \text{ K}$. To balance the heating by the X-rays from the reverse shock cooling has to be very efficient and may require enrichment by heavy elements. Observationally there is evidence for dust formation in the cool, dense shell from SN 1998S, where an infrared (IR) excess as well as a fading of the red side of the line profiles developed after about one year [131]. This became stronger with time at the same time as the dust temperature decreased. Dust condensation was also consistent with the different line profiles of the Ly α and H α lines, where the former developed a fading at earlier epochs compared to the latter [71]. Also the Type Ibn SN 2006jc had a similar evolution [139, 105] and is a good case for dust formation. In this case the reverse shock may already be in the metal enriched regions, promoting the dust formation.

The considerations so far apply to stars with mass loss rates $C_* \lesssim 10$, which includes most stars, including red supergiants with dense winds. At higher mass loss rates, like the ones relevant to LBV progenitors and Type IIin SNe, the observed X-ray emission from the forward shock comes to dominate the emission from the reverse shock. One reason is the absorption effect of the dense cool shell described above; another is that once the reverse shock becomes radiative, the luminosity rises proportional to density while the luminosity from the forward shock continues to grow as density squared. The emission from the forward shock is expected to be primarily free-free emission and the cooling time is

$$t_{\text{cool}} = \frac{3.5(n-3)}{(n-2)} C_*^{-1} \left(\frac{V_{\text{ej}}}{10^4 \text{ km s}^{-1}} \right)^3 \left(\frac{t}{\text{days}} \right)^2 \text{ days}. \quad (18)$$

The cooling time is therefore long except in cases of high mass loss density and slow shock wave; these properties are expected to go together.

At early epochs Compton cooling may also be important with a cooling rate

$$\frac{dE}{dt} = \frac{4kT_e\sigma_T}{m_e c^2} \frac{L(t)}{4\pi r^2} \quad (19)$$

where $L(t)$ is the luminosity of the SN. The cooling time then becomes

$$t_{\text{cool}} = 1.67 \left(\frac{V_{\text{ej}}}{10^4 \text{ km s}^{-1}} \right)^2 \left(\frac{t}{\text{days}} \right)^2 \left(\frac{L}{10^{42} \text{ erg s}^{-1}} \right)^{-1} \text{ days.} \quad (20)$$

which may be short for slow shocks and when the SN luminosity is high.

If the forward shock is cooling, the power emitted by the forward shock is

$$\begin{aligned} L_{\text{for}} &= 4\pi R_s^2 \frac{1}{2} \rho_{\text{cs}} V_s^3 = \frac{(n-3)^3}{2(n-2)^3} \frac{M V_{\text{ej}}^3}{u_w} \\ &= 3.2 \times 10^{41} \frac{(n-3)^3}{(n-2)^3} C_* \left(\frac{V_{\text{ej}}}{10^4 \text{ km s}^{-1}} \right)^3 \text{ erg s}^{-1}. \end{aligned} \quad (21)$$

The postshock gas temperature for the forward shock case is higher than for the reverse shock, giving an indication of the type of shock that is dominating the emission. These considerations can be applied to the case of SN 2010jl where the inference of $C_* \approx 10^3$ came from the bolometric light curve, which was dominated by optical radiation [73]. Application of Eq. (18) for $n = 8$ gives $t_{\text{cool}} = 0.35 V_{\text{ej},4}^{-3} C_*$ days, so with $C_* \approx 10^3$ and $V_s = 4000 \text{ km s}^{-1}$ gives ~ 5400 days for the duration of the radiative forward shock phase. The evolution of the luminosity in Eq. (21) is determined by the value of n , which relates to the deceleration of the interaction shell; $n = 7.6$, a reasonable value for the ejecta profile, is indicated for the first 300 days of evolution [73]

To relate the shock properties to the supernova model, we make the approximation that the supernova is described by an outer region with $n = 7$ and an inner region with a constant density; the two regions are separated at a transition velocity, V_t . The inner density profile is $\rho = At^{-3}$ and the outer profile is $\rho = At^{-3}(V/V_t)^{-7}$ where A and V_t are constants to be determined from the mass and energy: $V_t = 2.9 \times 10^3 E_{51}^{1/2} M_1^{-1/2} \text{ km s}^{-1}$ and $A = 1.13 \times 10^8 E_{51}^{-3/2} M_1^{5/2} \text{ g s}^3 \text{ cm}^{-3}$, where E_{51} is in units of 10^{51} ergs and M_1 in units of $10 M_\odot$. Substituting the outer density profile parameters in Eq. (7) gives

$$V = \frac{R_s}{t} = 1.48 \times 10^4 E_{51}^{2/5} M_1^{-1/5} C_*^{-1/5} t_{100}^{-1.5} \text{ km s}^{-1}, \quad (22)$$

where t_{100} is in units of 100 days. For $C_* = 10^3$, as inferred for SN 2010jl, the velocity coefficient is 3730 km s^{-1} . A somewhat higher energy or lower mass would bring the velocity into agreement with the value of $V_s = 4000 \text{ km s}^{-1}$ from X-ray observations [122, 25]. With these parameters, the interaction observed in SN 2010jl

for the first 300 days occurs in the outer, steep density power law region of the supernova; after 300 days, the more rapid decline can be attributed to a more rapidly decreasing density profile. Different parameters could give a situation in which the reverse shock wave has moved in to the flat part of the ejecta density distribution, which would also give a more rapid decline [122].

3.3 Asymmetries, shells and clumping

In view of the evidence for dense equatorial winds from red supergiant stars, Blondin, Lundqvist, & Chevalier [18] simulated the interaction of a supernova with such a wind. They found that for relatively small values of the angular density gradient, the asymmetry in the interaction shell is greater than, but close to, that expected from purely radial motion. If there is an especially low density close to the pole, the flow qualitatively changes and a protrusion emerges along the axis, extending to 2 – 4 times the radius of the main shell. Protrusions have been observed in the probable supernova remnant 41.9+58 in M82, although the nature of the explosion is not clear in this case [108].

In addition to asymmetric winds, there is evidence for supernova shock waves interacting with clumps of gas in the wind, as have been observed in some red supergiant winds. In some cases the clumps can be observed by their very narrow lines in supernova spectra, as in Type II_n supernovae. The velocity of a shock wave driven into a clump, V_c , can be estimated by approximate pressure balance

$$V_c \approx V_s \left(\frac{\rho_s}{\rho_c} \right)^{1/2}, \quad (23)$$

where V_s is the shock velocity in the smooth wind with density ρ_s and ρ_c is the clump density. The lower shock velocity and higher density can lead to radiative cooling of the clump shock although the main shock is non-radiative. Optical line emission of intermediate velocity observed in Type II_n (narrow line) supernovae like SN 1978K, SN 1988Z, and SN 1995N can be explained in this way [51, 52, 72].

The presence of many clumps can affect the hydrodynamics of the interaction. Jun, Jones, & Norman [87] found that propagation in a region with clumps gives rise to widespread turbulence in the shocked region between the forward shock and the reverse shock, whereas the turbulence is confined to a region near the reverse shock for the non-clump case (Fig. 2). Their simulations are for interaction with a constant density medium, but the same probably holds true for interaction with a circumstellar wind.

The interaction between the winds at the different evolutionary stages of the progenitor may result in dense shells around the SN. This may in particular be the case for a fast wind sweeping up a slower one. This may occur for a fast Wolf-Rayet wind sweeping up the slow red supergiant wind, or the wind from a blue supergiant sweeping up a slow wind, as may have been the case for SN 1987A [17].

The interaction of the SN ejecta with a dense shell depends on the ratio of the densities of the shell and the SN ejecta in the same way as was discussed for the clump interaction above (Eq. 23). The shells resulting from the interaction may in fact break up into clumps because of instabilities, as may have produced the clumps we now see as hotspots in SN 1987A.

For a high shell density a slow shock will be transmitted into the shell, while a reflected shock will propagate back into the SN ejecta and set up a reverse shock. The dynamics of this has been discussed in [43] where it is found that the ratio of the radius of the reverse shock to the contact discontinuity between shocked shell and shocked ejecta is given by

$$\frac{R_{\text{rev}}}{R_c} = \left(\frac{4n - 20}{4n - 15} \right)^{1/3} \quad (24)$$

For $n = 9$ one gets $R_{\text{rev}}/R_c = 0.91$.

4 Thermal emission from hot gas

4.1 *Optically thin emission*

The optical depth to electron scattering behind the circumstellar shock is

$$\tau_e = 0.18 C_* V_4^{-1} t_{\text{days}}^{-1}. \quad (25)$$

For mass loss rates $\lesssim 10^{-4} M_\odot \text{ yr}^{-1}$ and shock velocities $\gtrsim 10^4 \text{ km s}^{-1}$ the CSM will be optically thin and the radiation from the shocks will be only mildly affected. We therefore treat this case first. In Sect. 4.2 we discuss the optically thick case.

If the temperature in the post-shock gas is $\gtrsim 2 \times 10^7 \text{ K}$ free-free emission dominates the cooling and one can estimate the luminosity from the circumstellar and reverse shocks from

$$L_i = 4\pi \int \Lambda_{\text{ff}}(T_e) n_e^2 r^2 dr \approx \Lambda_{\text{ff}}(T_i) \frac{M_i \rho_i}{(\mu_e m_H)^2}. \quad (26)$$

where the index i refers to quantities connected either with the reverse shock or circumstellar shock. The density behind the circumstellar shock is $\rho_{\text{cs}} = 4 \rho_0 = \dot{M}/(\pi u_w R_s^2)$, while that behind the reverse shock is given by Eq. (13). The swept up mass behind the circumstellar shock is $M_{\text{cs}} = \dot{M} R_s / u_w$ and that behind the reverse shock $M_{\text{rev}} = (n - 4) M_{\text{cs}} / 2$. With $\Lambda_{\text{ff}} = 2.4 \times 10^{-27} \bar{g}_{\text{ff}} T_e^{0.5}$, we get

$$L_i \approx 3.0 \times 10^{39} \bar{g}_{\text{ff}} C_n C_*^2 \left(\frac{t}{10 \text{ days}} \right)^{-1} \text{ erg s}^{-1}, \quad (27)$$

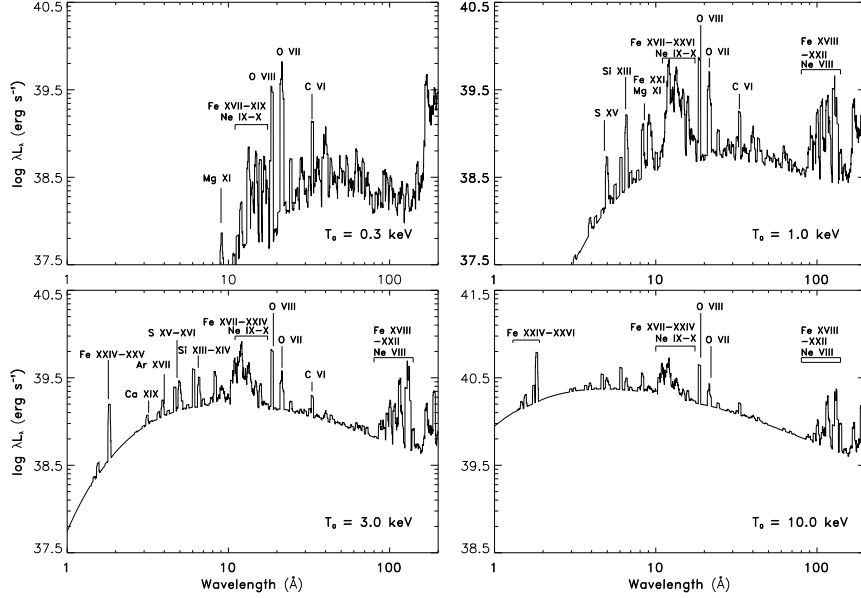


Fig. 3 Spectra, λL_λ , of radiative shocks with different reverse shock temperatures, $T_0 = 0.3, 1.0, 3.0,$ and 10.0 keV. The spectra are a convolution of spectra with decreasing temperature of the post-shock gas. All for solar composition. Note the increasing dominance of line emission for with decreasing temperature. From [120]. Reproduced with permission from Astronomy & Astrophysics, © ESO.

where \bar{g}_{ff} is the free-free Gaunt factor, including relativistic effects. For the reverse shock $C_n = (n-3)(n-4)^2/4(n-2)$, and for the circumstellar shock $C_n = 1$. This assumes electron-ion equipartition, which is highly questionable for the circumstellar shock (see Fig. 1). Because of occultation by the optically thick ejecta only half of the above luminosity escapes outward.

For temperatures $\lesssim 2 \times 10^7$ K behind the reverse shock the spectrum is dominated by line emission from metals (Fig. 3). An important point is that for a radiative shock the observed spectrum is formed in gas with widely different temperatures, varying from the reverse shock temperature down to $\sim 10^4$ K. A spectral analysis based on a one temperature model can be therefore misleading [120].

Another way of observing the hot gas is through the emission from collisionally heated dust grains in the gas [58]. Dust formation in the rapidly expanding ejecta is unlikely, so the forward shock front must be considered. Evaporation by the supernova radiation creates a dust-free zone around the supernova. The time for the supernova shock wave to reach the dust depends on the supernova luminosity and the shock velocity; it is probably at least several years. The infrared luminosity from dust can be up to ~ 100 times the X-ray luminosity of the hot gas for typical parameters, and the dust temperature is a measure of the density of the gas [58]. If the X-ray emission from a supernova like SN 1986J is from circumstellar clumps that

are out in the region where dust is present, there is the possibility of a large infrared luminosity.

4.2 *Optically thick emission*

Equation (25) shows that electron scattering can be a factor if the circumstellar density is large, e.g., the case of $C_* = 10^3$ for SN 2010jl. The lower shock velocity expected at high density also brings up the optical depth. The effect of significant Comptonization is a decrease in the energies of the most energetic photons. At each scattering, the photon wavelength is decreased by about $h/m_e c$, where h is Planck's constant and m_e is the electron mass. In each scattering the photon loses an energy $\Delta E \approx E^2/m_e c^2$. Approximating this as a continuous process, this energy will be lost in a time $\sim \lambda_{\text{mfp}}/c$, where λ_{mfp} is the mean free path. Therefore a photon with initial energy E_0 will after a time t have an energy given by

$$\int_0^t \frac{dt'}{\lambda_{\text{mfp}}/c} = \int_{E_0}^E \frac{m_e c^2}{E^2} dE \quad (28)$$

or

$$\frac{ct}{\lambda_{\text{mfp}}} = m_e c^2 \left(\frac{1}{E} - \frac{1}{E_0} \right) \approx \frac{m_e c^2}{E}. \quad (29)$$

In the time t the number of scatterings, N , is given by $t = N\lambda_{\text{mfp}}/c \approx \tau_e^2 \lambda_{\text{mfp}}/c$. Therefore,

$$E \approx \frac{m_e c^2}{\tau_e^2} = \frac{511}{\tau_e^2} \text{ keV}. \quad (30)$$

A collisionless shock can form with τ_e as high as c/V_s , so there is the possibility of setting a strong upper limit on the X-ray spectrum.

The electron scattering opacity for a medium with cosmic abundances and ionized H and He is $0.34 \text{ cm}^2 \text{ g}^{-1}$, while the photoabsorption opacity is $106 E_{\text{keV}}^{-8/3} (Z/Z_\odot) \text{ cm}^2 \text{ g}^{-1}$, where Z is the metallicity. The two opacity sources are comparable for $E \approx 10 \text{ keV}$. If $\tau_e \approx 1$, photons near 10 keV can escape, but lower energy photons are absorbed. This was the case in the early observations of SN 2010jl [25, 122] (see Section 6.4).

Photoabsorption does not occur if the surrounding circumstellar medium is completely ionized by the supernova emission. If the supernova is in the cooling regime, a $10,000 \text{ km s}^{-1}$ shock wave is capable of completely ionizing the surrounding medium, but a 5000 km s^{-1} shock wave is not [42]. This is consistent with the absorption observed in SN 2010jl. At lower densities, complete ionization is more easily achieved, which is consistent with the early soft X-ray emission observed from SN 1993J [76].

4.3 Reprocessing of X-rays

4.3.1 Ionization of the circumstellar gas

The earliest form of circumstellar interaction occurs at shock break-out. As the shock approaches the surface, radiation leaks out on a time scale from seconds to hours, depending on the size of the progenitor. Matzner & McKee [106] have found approximate solutions for the effective temperature and energy of the shock break-out for both convective and radiative envelopes, approximated as polytropes. For the convective case (applicable to red supergiants) they find

$$T_{\max} \approx 5.6 \times 10^5 \left(\frac{R_*}{500 R_\odot} \right)^{-0.54} \text{ K} \quad (31)$$

$$E \approx 1.7 \times 10^{48} \left(\frac{R_*}{500 R_\odot} \right)^{1.74} \text{ ergs}, \quad (32)$$

while for the radiative case (blue supergiants, WR stars) they find

$$T_{\max} \approx 1.6 \times 10^6 \left(\frac{R_*}{50 R_\odot} \right)^{-0.48} \text{ K} \quad (33)$$

$$E \approx 7.6 \times 10^{46} \left(\frac{R_*}{50 R_\odot} \right)^{1.68} \text{ ergs}. \quad (34)$$

The color temperature, which determines the ionization, may differ from T_{\max} because of scattering and other effects, but these expressions show the strong dependence on the radius of the progenitor, R_* , for both the temperature and total energy of the shock break-out. This is also the case for the duration of the burst, which is usually set by the light travel time over the progenitor, $\sim R_*/c$, which varies from seconds to hours for different types of progenitors [106].

This burst of EUV (extreme ultraviolet) and soft X-rays ionizes and heats the circumstellar medium on a time scale of a few hours. In addition, the momentum of the radiation may accelerate the circumstellar gas to a high velocity. Most of the emission at energies $\gtrsim 100$ eV is emitted during the first few hours, and after 24 hours little ionizing energy from the shocked ejecta remains.

In addition to the initial burst, the X-ray emission from the shocks ionizes and heats both the circumstellar medium and the SN ejecta as it propagates through the CSM. Observationally, these components are easily distinguished by the different velocities. The circumstellar component is expected to have velocities typical of the progenitor winds, i.e., $\lesssim 1000$ km s⁻¹, while the ejecta have considerably higher velocities. The density is likely to be of the order of the wind density $10^5 - 10^7$ cm⁻³, or higher if clumping is important. The ionizing X-ray flux depends strongly on how much of the flux from the reverse shock can penetrate the cool shell, or in the case of extreme mass loss rates the CSM gas. The state of ionization in the circumstellar gas is characterized by the value of the ionization

parameter, $\zeta = L_{\text{cs}}/(r^2 n) = 10^2 (L_{\text{cs}}/10^{40} \text{ erg s}^{-1})(r/10^{16} \text{ cm})^{-2}(n/10^6 \text{ cm}^{-3})^{-1}$ [88]. The comparatively high value of $\zeta \approx 10 - 10^3$ explains the presence of narrow coronal lines of [Fe V-XIV] seen in objects like the Type II_n SNe 1995N [72], 1998S [61], 2006jd [143] and 2010jl [73].

The radiative effects of the soft X-ray burst were clearly seen from the ring of SN 1987A, where a number of narrow emission lines from highly ionized species, like C III-IV, N III-N V, and O III-IV were first seen in the UV [70]. Later, a forest of lines came to dominate also the optical spectrum (see e.g., [77]). Imaging with HST (e.g., [85, 20]) showed that the lines originated in the now famous circumstellar ring of SN 1987A at a distance of ~ 200 light days from the SN. The presence of highly ionized gas implied that the gas must have been ionized and heated by the radiation at shock break-out. Because of the finite light travel time across the ring, the observed total emission from the ring is a convolution of the emission at different epochs from the various part of the ring. Detailed modeling [94] shows that while the ionization of the ring occurs on the time scale of the soft X-ray burst, the gas recombines and cools on a time scale of years, explaining the persistence of the emission decades after the explosion. The observed line emission provides sensitive diagnostics of both the properties of the soft X-ray burst, and the density, temperature and abundances of the gas in the ring. In particular, the radiation temperature must have reached $\sim 10^6$ K, in agreement with the modeling of the shock break-out. The strong N III] relative to the C III] and O III] lines indicated a strong N enrichment from CNO processing, as well as an enhanced He abundance.

The soft X-ray burst may also pre-accelerate the gas in front of the shock. In the conservative case that Thompson scattering dominates, the gas immediately in front of the shock will be accelerated to

$$V_{\text{acc}} = 1.4 \times 10^3 \left(\frac{E}{10^{48} \text{ ergs}} \right) \left(\frac{V_s}{1 \times 10^4 \text{ km s}^{-1}} \right)^{-2} \left(\frac{t}{\text{days}} \right)^{-2} \text{ km s}^{-1}, \quad (35)$$

where E is the total radiative energy in the burst. If the gas is pre-accelerated, the line widths are expected to decrease with time. After about one expansion time ($\sim R_p/V$) the reverse and circumstellar shocks are fully developed, and the radiation from these will dominate the properties of the circumstellar gas.

The increasing blue-shifts with time of the H α line in SN 2010jl has been proposed to arise as a result of radiative acceleration by the extremely large radiated energy ($\gtrsim 6 \times 10^{50}$ ergs) [73], although part of this may also result from the dense shell [53].

4.3.2 Emission from the SN ejecta and cool, dense shell

The ingoing X-ray flux from the reverse shock ionizes the outer parts of the ejecta [66, 67]. The state of highest ionization therefore is close to the shock, with a gradually lower degree of ionization inwards. Unless clumping in the ejecta is important, the ejecta density is $\sim 10^6 - 10^8 \text{ cm}^{-3}$ during the first year. In the left panel of Fig.

4 we show temperature and ionization structure of the ejecta for a reverse shock velocity of 1300 km s^{-1} , as well as the emissivity of the most important lines. The ejecta velocity was $1.3 \times 10^4 \text{ km s}^{-1}$ and the ejecta gradient $n = 12$. The temperature of the outer ejecta close to the shock is $\sim 3 \times 10^4 \text{ K}$, decreasing inwards in. Most of the emission here is emitted as UV lines of highly ionized ions, like $\text{Ly}\alpha$, C III-IV, N III-V, and O III-VI. Inside the ionized shell there is an extended partially ionized zone, similar to that present in the broad emission line regions of AGN's. Most of the emission here comes from Balmer lines.

As we have already discussed, the outgoing flux from the reverse shock is to a large extent absorbed by the cool shell between reverse shock and the contact discontinuity if radiative cooling has been important. The whole region behind the reverse shock is in approximate pressure balance, and the density of this gas is therefore a factor $\sim 4T_{\text{rev}}/T_{\text{cool}} \approx 10^3 - 10^4$ higher than that of the ejecta. Because of the high density, the gas is only partially ionized and the temperature only $(5 - 8) \times 10^3 \text{ K}$. Most of the emission comes out as Balmer lines, Mg II and Fe II lines (Fig. 4, right panel). The thickness of the emitting region is also very small, $\sim 3 \times 10^{12} \text{ cm}$. In one dimensional models, the velocity is marginally smaller than the highest ejecta velocities. Instabilities in the shock are, however, likely to erase this difference.

An important diagnostic of the emission from the cool shell and the ejecta is the $\text{H}\alpha$ line [37]. This line arises as a result of recombination and collisional excitation. In [38], it is estimated that $\sim 1\%$ of the reverse shock luminosity is emitted as $\text{H}\alpha$, fairly independent of density and other parameters. Observations of this line permit us to follow the total luminosity from the reverse shock, complementary to the X-ray observations. In SN 1993J, the $\text{H}\alpha$ line had the box-like shape that is expected for shocked, cooled ejecta [102, 104]. The top of the line showed structure that varied with time; this could be related to hydrodynamic instabilities of the reverse shocked gas.

5 Non-thermal emission from relativistic particles

5.1 Particle acceleration and magnetic field amplification in shocks

Although the basic principles of particle acceleration in shocks, based on first order Fermi acceleration across a shock discontinuity ('diffusive shock acceleration'), were proposed in the 1970s, e.g., [92], there are many aspects that are not well understood. This includes in particular the efficiency of the acceleration mechanism for ions and electrons and the strength of the magnetic field. The energy density of these are usually parameterised in terms of the shock energy density, $\rho_{\text{cs}}V_s^2$, as ϵ_B , ϵ_e and ϵ_{ion} . Based on equipartition arguments these are often assumed to be of the order of ~ 0.1 , but without strong observational support. For interpreting radio and X-ray observations, these parameters are, however, crucial.

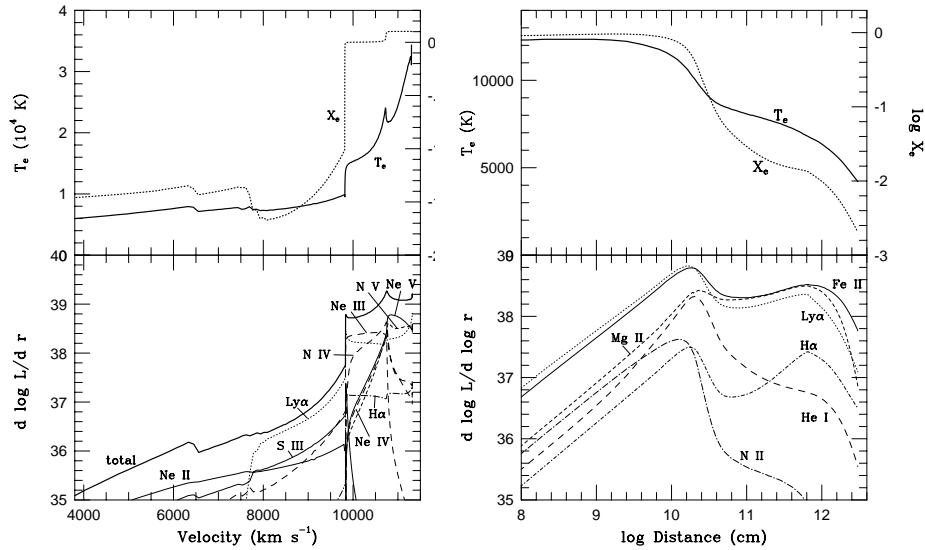


Fig. 4 Structure of the ejecta (left panels) and cool shell (right panels) ionized by the reverse shock at 500 days for parameters appropriate to SN 1993J ($\dot{M} = 5 \times 10^{-5} M_{\odot} \text{ yr}^{-1}$ for $u = 10 \text{ km s}^{-1}$). Upper panels show the temperature and ionization of the ejecta and the cool shell, while the lower panels show the corresponding luminosities per unit distance. Note the different length scales in the two panels. The ejecta region has low density, high temperature and ionization, while the cool shell has a high density, is extremely thin, has a low temperature, and is only partially ionized.

Except for the general spectrum, which mainly depends on the kinematics of the shock, in particular, the compression ratio, the microphysics determining the injection efficiency and magnetic field amplification are determined by a complex interplay between different plasma instabilities and their implications for the relativistic particles. For quantitative results advanced numerical simulations are therefore needed. A main complication here is the different physical scales which are important, including the electron skin depth, the gyro radii of the electrons and ions and the scale of the acceleration region. These differ by many orders of magnitude and different approximations are needed. Here we only mention some recent important results. For a general review of the physics of collisionless shocks see e.g., [21, 97].

One approach, which is well suited for studying the ion component, is known as hybrid-PIC simulations. In these the ions are treated kinetically and electrons as a neutralizing fluid. This allows an accurate treatment of the acceleration of the ions (i.e., cosmic rays) but not the electrons. The advantage is that the simulation box can be a factor $(m_p/m_e)^{1/2} = 43$ larger compared to the case when electrons are also included kinetically.

Using this approach Caprioli & Spitkovsky [22, 23, 24] have made an extensive study of the acceleration efficiency and magnetic field amplification of shocks with different Mach numbers, $M = 5 - 50$, and obliquity. These are the most advanced simulations to date and we discuss some of the main results.

The particles are injected with a thermal spectrum, but soon develop a non-thermal tail with a power law slope $dN(p)/dp \propto p^{-2}$, where p is the momentum of the particles, as expected from diffusive shock acceleration. The temperature was $\sim 20\%$ of that without any cosmic ray acceleration, with the rest of the energy residing in the cosmic rays. The escaping ions show a clear separation between the thermal and non-thermal particles at an energy $\sim (4 - 5)m_p V_s^2/2$.

Independent of the Mach number, Caprioli & Spitkovsky find a significant drop in the acceleration efficiency for shocks with obliquity $\theta < 45^\circ$, and it is close to zero for nearly perpendicular shocks ($\theta > 60^\circ$). The efficiency in general increases with the Mach number, but is in the range $\epsilon_{\text{ion}} = 5 - 15\%$.

The magnetic field amplification is induced by the cosmic ray streaming [8, 9] and therefore depends on both the Mach number and obliquity, as discussed above. The largest amplifications therefore occur for quasi-parallel shocks with high Mach numbers. For $\theta = 90^\circ$ and $M = 50$ the amplification is ~ 10 above the background field, and is approximately proportional to M for the range studied.

An efficient acceleration of cosmic rays may have consequences for the shock structure, with a weak sub-shock from the cosmic ray precursor ahead of the main shock [55, 86]. This will in turn affect the spectra of the accelerated electrons. Low energy electrons will then only scatter across part of the shock, with a smaller compression, while the high energy particles would scatter across the full shock and therefore feel the full compression. This would therefore result in a steep low energy spectrum and a flatter high energy spectrum, similar to that without cosmic rays. In the hybrid simulations discussed above there is a steeper section of the particle spectrum close to the shock, joining the thermal and non-thermal regions. It is not clear if this would result in a steeper integrated synchrotron spectrum. The total compression ratio in the quasi-parallel case is ~ 4.3 , somewhat larger than in the test-particle case.

Recently, full PIC (particle-in-cell) simulations have allowed a study of the simultaneous acceleration of both electrons and protons in a collisionless shock [125] (Fig. 5). Although they are only one-dimensional (1D) in space for computational reasons, they include all components of velocity and magnetic field. To limit the effect of the different gyro radii of the electrons and protons the proton to electron mass was set to $m_p/m_e = 100$.

As above, the streaming of the protons excites magnetic turbulence in the upstream plasma by the non-resonant Bell instability [8], which leads to an amplification by a factor of about two in the upstream plasma. This turbulence is then amplified further at the shock transition.

The acceleration of the electrons initially occurs by shock drift acceleration across the shock and scattering by the magnetic turbulence. As the momentum increases this transitions into a standard diffusive shock acceleration process. In the simulations both the electrons and ions relax to the same power law spectra, with a

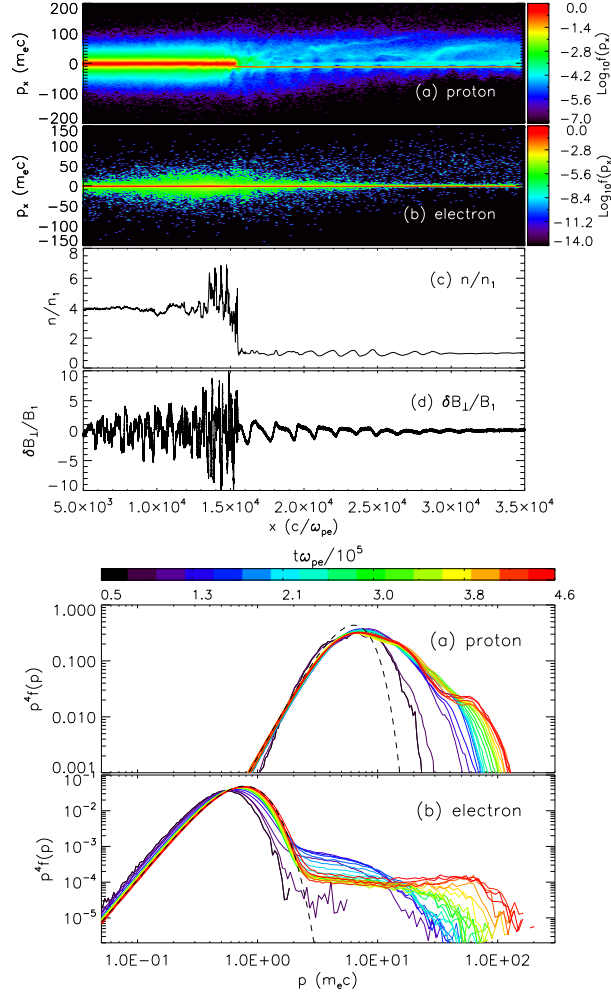


Fig. 5 Upper figure: Upper panels: Momentum distributions of electrons and protons along the x-axis in the pre- and post-shock regions. Middle panel: Density. Lower panel: The transverse magnetic field along the same axis. Note the increased B-field in the pre-shock region due to the Bell-instability and the continued amplification behind the shock. Lower figure: Evolution in time of the electron and proton distributions at a point behind the shock. Note that $p^4 f(p) = p^2 dN(p)/dp$ is plotted. The flat electron spectrum above $p \sim 3m_e c$ has $dN(p)/dp \propto p^{-2}$ in agreement with diffusive shock acceleration. With permission from [125].

slope close to $dN(p)/dp \propto p^{-2}$. At non-relativistic energies this results in an energy spectrum $dN/dE \propto E^{-3/2}$ and in the relativistic regime $dN/dE \propto E^{-2}$. The similar spectra result in an energy independent ratio of $N_e/N_p \approx 10^{-3} - 10^{-2}$ between the electrons and protons, with the ratio increasing with shock velocity.

The general result that efficient acceleration only seems to occur for quasi-parallel shocks, i.e., where the B-field is approximately aligned with the direction of the shock velocity, may have consequences for shocks in a stellar wind from a rotating progenitor star, where the magnetic field may have the topology of a Parker spiral, causing the shock to be closer to perpendicular with respect to the magnetic field direction. Small scale turbulence and irregularities may, however, result in a situation intermediate between the two cases.

Although there has been impressive recent advances, especially connected to these kinetic simulations, many questions remain. This includes the dependence on the shock velocity, the efficiency for perpendicular shocks, the level of the magnetisation, the dependence on the assumed proton to electron mass ratio, non-linear effects from the cosmic ray pressure, etc.

5.2 *Optically thin synchrotron emission*

The most important emission mechanism of the non-thermal electrons is usually synchrotron emission. This mechanism is discussed in many textbooks e.g., [92, 132] and here only a few important results are given.

A relativistic electron with a Lorentz factor γ in a magnetic field B will radiate in a narrow frequency range around the critical frequency

$$\nu_c = \frac{eB}{m_e c} \gamma^2 = 1.76 \times 10^7 B \gamma^2 \text{ Hz}, \quad (36)$$

where an average over pitch angles has been taken. Here e and m_e are the electron charge and mass, respectively, and c the velocity of light. The total energy lost by the electron is

$$\frac{dP}{dt} = \frac{4}{3} \sigma_T c \gamma^2 \frac{B^2}{8\pi}. \quad (37)$$

where σ_T is the Thompson cross section. We assume that the electrons are created with a power law distribution of relativistic electrons, $dN/dE = N_0 E^{-p}$, where $E = \gamma m_e c^2$. Note that p is here and from now on the spectral index of the electron distribution, not momentum as in the previous section. Approximating the spectrum of an individual electron with a delta function and using Eqs (36) and (37), the emissivity per frequency at frequency ν becomes

$$j(\nu) d\nu \approx \frac{1}{4\pi} \frac{dN(E)}{dE} \frac{dP}{dt} dE = \text{const. } N_0 B^{(p+1)/2} \nu^{-(p-1)/2} d\nu. \quad (38)$$

It is a power law with spectral index $\alpha = (p-1)/2$ determined by the power law index of the non-thermal electrons.

The synchrotron cooling time of an electron is

$$t_{\text{synchro}} = \frac{\gamma m_e c^2}{dP/dt} = 6\pi \frac{m_e c}{\sigma_T} B^{-2} \gamma^{-1} = 7.7 \times 10^8 B^{-2} \gamma^{-1} \text{ s} \quad (39)$$

or in terms of the emitted frequency

$$t_{\text{synchro}} = 6\pi \frac{(em_e c)^{1/2}}{\sigma_T} B^{-3/2} \nu^{-1/2} = 3.2 \times 10^7 B^{-3/2} \nu_{10}^{-1/2} \text{ s.} \quad (40)$$

where $\nu_{10} = \nu/10$ GHz.

It is common to relate the magnetic field to the mass loss rate parameters by scaling the magnetic energy density to the shock energy density, $\rho_{\text{cs}} V_s^2$. With the scaling parameter ϵ_B we get

$$\frac{B^2}{8\pi} = \epsilon_B \rho_{\text{cs}} V_s^2 = \epsilon_B \frac{\dot{M}}{4\pi u_w r^2} V_s^2 = \epsilon_B \frac{\dot{M}}{4\pi u_w t^2}. \quad (41)$$

We then obtain

$$B = 4.1 \epsilon_B^{1/2} C_*^{1/2} \left(\frac{t}{10 \text{ days}} \right)^{-1} \text{ G} \quad (42)$$

and

$$\frac{t_{\text{synchro}}}{t} = 4.4 \epsilon_B^{-3/4} C_*^{-3/4} \left(\frac{t}{10 \text{ days}} \right)^{1/2} \nu_{10}^{-1/2}. \quad (43)$$

If relativistic electrons are created by the acceleration process with a spectrum $N_0 E^{-p}$ according to Eq. (39) they will have a lifetime proportional to E^{-1} . For the electrons for which the cooling time is short compared to the time since they were created, the integrated electron spectrum of the source is proportional to $N_0 E^{-p-1}$. From Eq. (38) the source then has a synchrotron spectrum $j(\nu) \propto \nu^{-p/2}$, i.e., steeper by 1/2 in the spectral index.

5.3 Inverse Compton X-ray emission

Besides synchrotron emission, inverse Compton emission may be important for the UV and X-ray emission. The most important sources of photons are the ones from the photosphere and from any optical/UV emission from the shock region. The cooling time scale of the same non-thermal electrons emitting the synchrotron emission is identical to Eq. (37), with $B^2/8\pi$ replaced by the radiation density, $U = L/4\pi r^2 c$, so

$$\frac{t_{\text{Compton}}}{t} = 0.85 \epsilon_B^{1/4} C_*^{1/4} \left(\frac{L}{10^{42} \text{ erg s}^{-1}} \right)^{-1} \left(\frac{V_s}{10^4 \text{ km s}^{-1}} \right)^2 \left(\frac{t}{10 \text{ days}} \right)^{1/2} \nu_{10}^{-1/2}. \quad (44)$$

The ratio between the synchrotron and Compton cooling time scales is

$$\frac{t_{\text{synchro}}}{t_{\text{Compton}}} = \frac{2L}{cB^2r^2} = 5.2 \times 10^{-2} \epsilon_B^{-1} C_*^{-1} \left(\frac{L}{10^{42} \text{ erg s}^{-1}} \right) \left(\frac{V_s}{10^4 \text{ km s}^{-1}} \right)^{-2}. \quad (45)$$

Inverse Compton cooling is therefore mainly important for the cooling at early phases when the luminosity is high, for low mass loss rates and for slow shocks. Because the cooling time scale has the same γ^{-1} dependence as the synchrotron cooling, the effect on the electron distribution and emitted spectrum will be the same for energies and frequencies where the cooling time is short, i.e., $F_\nu \propto \nu^{-p/2}$.

For a Compton dominated shock the radio spectrum and light curve is given by

$$F_\nu(t) \propto \epsilon_B^{-1} C_*^{-1} L(t)^{-1} t^{m-p/2} \nu^{-p/2}. \quad (46)$$

[69, 120]. The radio light curve is therefore inversely correlated with the optical light curve, which may result in a flattening of the radio light curve at the time of optical peak for high frequencies [41].

The energy lost by the relativistic electrons is transferred to the soft photons, which will be scattered to an energy $E_x \sim \gamma^2 E_0$, where E_0 is the initial energy of the photon. For a SN the main soft photon flux is in the optical. The Compton scattered photons are then typically in the X-rays. The total energy loss of the electron is $dP/dt = 4/3 \sigma_T c U_{\text{rad}} \gamma^2$, same as in Eq. (37) with $B^2/8\pi$ replaced by U_{rad} . With a non-thermal electron spectrum $dN/dE = N_0 E^{-p}$, we get for the inverse Compton spectrum at energy E_x

$$\frac{dF}{dE_x} dE_x \approx 4\pi r^2 \frac{dP}{dt} \frac{dN}{dE} dE = \frac{16\pi r^2}{3} \sigma_T c U_{\text{rad}} \gamma^2 \frac{dN}{dE} dE.$$

With a non-thermal electron spectrum $dN/dE = N_0 E^{-p}$ we get

$$\frac{dF}{dE_x} dE_x = \frac{16\pi r^2}{3} \sigma_T c U_{\text{rad}} N_0 (m_e c^2)^{-2} E^{-p+2} dE.$$

Using $E_x \approx \gamma^2 E_0 = (E/m_e c^2)^2 E_0$ one finds for the inverse Compton spectrum at energy E_x

$$\frac{dF}{dE_x} dE_x = \frac{8\pi r^2}{3} \sigma_T c \frac{U_{\text{rad}}}{E_0} N_0 (m_e c^2)^{-2} \left(\frac{E_x}{E_0} \right)^{-(p-1)/2} (m_e c^2)^{-p+1} dE_x.$$

Averaging over a blackbody spectrum $E_0 \approx 3.6kT_{\text{bb}}$ [62]. Far from the source of the soft photons $U_{\text{rad}} = L/4\pi r^2 c$, so finally

$$\frac{dF(E_x)}{dE_x} = \frac{2}{3} \sigma_T L(t) N_0 (m_e c^2)^{-p-1} (3.6kT_{\text{bb}})^{(p-3)/2} E_x^{-(p-1)/2}. \quad (47)$$

The spectrum is therefore the same as the corresponding synchrotron spectrum from the same electron distribution and the flux is directly proportional to the luminosity of the soft photon source. Also note the insensitivity to the temperature of the blackbody radiation for $p \approx 3$.

Compton scattering is also important as a cooling process of the *thermal* electrons of the circumstellar shock. In contrast to free-free and line cooling this does not depend on the density and only on the radiation density of the photons from the photosphere. Heating by the hard radiation from the shocks may be important for both the CSM and the outer layers of the SN ejecta.

The average energy transfer rate of a photon with energy $h\nu$ interacting with thermal electrons with temperature T_e is

$$\Delta E = \frac{h\nu}{m_e c^2} (4kT_e - h\nu) \quad (48)$$

Depending on the energy of the photon the radiation relative to the temperature of the electrons can therefore act as either a heating or cooling process.

The photospheric photons have energies $\sim 3 kT_{eff} \approx 1 - 10$ eV. A fraction τ_e^N of the photospheric photons will scatter N times in the hot gas. In each scattering the photon increases its energy by a factor $\Delta\nu/\nu \approx 4 kT_e/m_e c^2 \gtrsim 1$. The multiple scattering creates a power law continuum that may reach as far up in energy as the X-ray regime. Typically, $1 \lesssim \alpha \lesssim 3$. This type of emission may have been observed in the ultraviolet emission from SN 1979C [66]. For $T_e \gtrsim 10^9$ K relativistic effects become important and considerably increase the cooling [93].

5.4 *The radio spectrum including absorption processes*

Unambiguous evidence for the presence of relativistic electrons comes from radio observations of SNe. A characteristic is the wavelength-dependent turn-on of the radio emission [141], first seen at short wavelengths, and later at longer wavelengths. This behaviour is interpreted as a result of decreasing absorption due to the expanding emitting region [29].

Depending on the magnetic field and the density of the circumstellar medium, the absorption may be produced either by free-free absorption in the surrounding thermal gas, or by synchrotron self-absorption by the same electrons that are responsible for the emission. The relativistic electrons are believed to be produced close to the interaction region, which provides an ideal environment for the acceleration of relativistic particles. As discussed above, the details of the acceleration and injection efficiency are still not well understood. Here we just parameterize the injection spectrum with the power law index p_i and an efficiency, η , in terms of the post-shock energy density. Without radiation or collisional losses the spectral index of the synchrotron emission will then be $F_\nu \propto \nu^{-\alpha}$ with $\alpha = (p_i - 1)/2$. As discussed earlier, diffusive acceleration predicts that $p_i = 2$ in the test particle limit, but can be steeper if the particle acceleration is very efficient and nonlinear effects are important.

For free-free absorption, the optical depth $\tau_{ff} = \int_{R_s}^{\infty} \kappa_{ff} n_e n_i dr$ from the radio emitting region close to the shock through the circumstellar medium decreases as the shock wave expands, explaining the radio turn-on. Assuming a fully ionized and

a temperature T_e wind with constant mass loss rate and velocity, so that Eq. (2) applies, the free-free optical depth at wavelength λ is

$$\tau_{\text{ff}}(\lambda) \approx 6.0 \times 10^2 \left[1 + \frac{n(\text{He})}{n(\text{H})} \right] \lambda^{2.118} C_*^2 \left(\frac{T_e}{10^5 \text{ K}} \right)^{-1.323} \left(\frac{V_s}{10^4 \text{ km s}^{-1}} \right)^{-3} \left(\frac{t}{\text{days}} \right)^{-3}, \quad (49)$$

including the slight variation of the Gaunt-factor with temperature and wavelength. One should also note that especially for stars that have undergone strong mass loss the helium to hydrogen ratio may have been substantially enhanced compared to the solar value.

From the radio light curve, or spectrum, the epoch of $\tau_{\text{ff}} = 1$ can be estimated for a given wavelength, and from the line widths in the optical spectrum the maximum expansion velocity, V , can be obtained. From $t[\tau(\lambda)_{\text{ff}} = 1]$ the mass loss parameter C_* and therefore the ratio \dot{M}/u_w can be calculated. Because $\dot{M}/u_w \propto T_e^{0.66} x_e^{-1}$, errors in T_e and x_e may lead to large errors in \dot{M} . Both T_e and x_e are set by the radiation from the SN and have to be estimated from models of the ionization and heating of the circumstellar medium.

Calculations show that the radiation from the shock break-out (Sect. 4.3.1) heats the gas to $T_e \approx 10^5$ K [93]. T_e then decreases with time, and after a year $T_e \approx (1.5 - 3) \times 10^4$ K. In addition, the medium may recombine, which further decreases the free-free absorption. If the shock breakout radiation is soft and the X-ray flux from the continuing circumstellar interaction is weak, heating resulting from the free-free absorption may determine the temperature, giving a temperature $\lesssim 10^5$ K [16]. We also note that because $\tau_{\text{ff}} \propto n_e n_i$ Eq. (49) may lead to an overestimate of \dot{M}/u_w if the medium is clumpy.

Under many circumstances (see below), synchrotron self-absorption (SSA) by the same relativistic electrons emitting the synchrotron radiation is important [135, 32, 69]. In Eq. (38) we gave an approximate expression for the synchrotron emissivity. Here we give the exact expressions for the emission and for the absorption effects, assuming a constant power law, p , for the electrons and a randomly oriented magnetic field. For a detailed account of synchrotron processes see e.g., [32, 124, 132].

The emissivity is given by

$$j(\nu) = c_{\text{em}}(p) B^{(p+1)/2} N_0 \left(\frac{\nu}{\nu_0} \right)^{-(p-1)/2} \quad (50)$$

where $\nu_0 = 1.253 \times 10^{19}$ Hz and

$$c_{\text{em}}(p) = 4.133 \times 10^{-24} \left(\frac{p+7/3}{p+1} \right) \Gamma \left(\frac{3p-1}{12} \right) \Gamma \left(\frac{3p+7}{12} \right) \times \Gamma \left(\frac{p+5}{4} \right) \Gamma \left(\frac{p+7}{4} \right)^{-1}. \quad (51)$$

Table 1 Synchrotron constants in c.g.s. units for values of the energy power law index p for emission and absorption (Eqs. 50 and 52).

p	1.0	1.5	2.0	2.5	3.0	3.5
$c_{\text{em}}/10^{-23}$	3.8359	1.6954	0.9874	0.6688	0.5013	0.4050
$c_{\text{abs}}/10^{-41}$	8.4809	6.7024	5.7410	5.2179	4.9697	4.9198

The self absorption opacity, $\kappa(\nu)$, can be obtained from the emissivity and detailed balance (see e.g., [124, 132]). Under the same assumptions as above for the emissivity one obtains

$$\kappa(\nu) = c_{\text{abs}}(p) N_0 B^{(p+2)/2} \left(\frac{\nu}{\nu_0} \right)^{-(p+4)/2}, \quad (52)$$

where

$$c_{\text{abs}}(p) = 1.183 \times 10^{-41} (p + 10/3) \Gamma\left(\frac{3p+2}{12}\right) \Gamma\left(\frac{3p+10}{12}\right) \times \Gamma\left(\frac{p+6}{4}\right) \Gamma\left(\frac{p+8}{4}\right)^{-1}. \quad (53)$$

Values for c_{em} and c_{abs} for selected values of p are given in Table 1.

Taking the self-absorption of the synchrotron emission into account, the observed flux is

$$F_{\nu} = \frac{\pi R_s^2}{D^2} S(\nu) [1 - \exp(-\tau(\nu))], \quad (54)$$

where

$$\tau(\nu) = \int_0^s \kappa(\nu) ds \approx \kappa(\nu) s \quad (55)$$

is the optical depth of a slab with thickness s , and $S(\nu)$ is the source function

$$S(\nu) = \frac{j(\nu)}{\kappa(\nu)} = \frac{c_{\text{em}}(p)}{c_{\text{abs}}(p)} B^{-1/2} \left(\frac{\nu}{\nu_0} \right)^{5/2}. \quad (56)$$

For a spherical source the effective thickness s can be taken to be equal to the ratio of the emitting volume, $4\pi R_s^3 f/3$ and the projected area πR_s^2 , where f is the volume filling factor of the synchrotron emitting volume.

In the optically thick limit we therefore have

$$F_{\nu}(\nu) \approx \frac{\pi R_s^2}{D^2} \frac{c_{\text{em}}}{c_{\text{abs}}} \left(\frac{\nu}{\nu_0} \right)^{5/2} B^{-1/2}, \quad (57)$$

independent of N_0 . A fit of this part of the spectrum therefore gives the quantity $R_s^2 B^{-1/2}$.

In the optically thin limit $F(\nu) \propto j(\nu) \propto R_s^2 B^{(p+1)/2} N_0 \nu^{-(p-1)/2}$. The spectrum will therefore have a break at the frequency where $\nu(\tau \approx 1)$. The condition $\tau(\nu) = \kappa(\nu)s = 1$ with $\kappa(\nu)$ from Eq. (52) therefore gives a second condition on $B^{(p+2)/2} N_0 R_s^3$. Now, if $R_s(t)$ is known in some independent way, one can determine both the magnetic field and the column density of relativistic electrons, independent of assumptions about equipartition, etc.

In some cases, most notably for SN 1993J, the shock radius, R_s , can be determined directly from very long baseline interferometry (VLBI) observations. If this is not possible, an alternative is from observations of the maximum ejecta velocity seen in, e.g., the $H\alpha$ line, which should reflect the velocity of the gas close to the shock. Because the SN expands homologously, $R_s = V_{\max}t$. A fit of the spectrum at a given epoch can therefore yield both B and N_{rel} independently. From observations at several epochs the evolution of these quantities can then be determined [69].

Even if R_s , and therefore V_s , is not known a useful estimate for these quantities can be derived from the observation of the flux and time of the peak of the radio light curves for a given frequency [32]. With $s = 4fR_s/3$ and $\tau(\nu) \approx \kappa(\nu)s \approx 1$, with $\kappa(\nu)$ from Eq. (52), this gives a relation between N_0 , B_{peak} and $R_{s \text{ peak}}$. If we assume an electron spectrum with lower energy limit E_{\min} , which we can take to be equal to $\sim m_e c^2$, one gets for the total energy density $U_e = N_0 E_{\min}^{-p+2}/(p-2)$. Finally, we assume a constant ratio between this and the magnetic energy density equal to ζ , we get $N_0 = \zeta(p-2)B^2 E_{\min}^{p-2}/8\pi$. From Eq. (52) we then get

$$B = \left[\frac{6\pi}{f R_s c_{\text{abs}} (p-2) \zeta E_{\min}^{p-2}} \right]^{2/(6+p)} \left(\frac{\nu}{\nu_0} \right)^{(p+4)/(p+6)}. \quad (58)$$

Estimating the flux at the peak with the optically thick expression, Eq. (57), and using the above expression for B and solving for R_s one gets

$$R_s(t_{\text{peak}}) = \left(\frac{c_{\text{abs}}}{\pi} \right)^{(5+p)/(13+2p)} \left[\frac{6}{f(p-2)\zeta E_1^{p-2}} \right]^{1/(13+2p)} \times \left[\frac{F_{\nu}(t_{\text{peak}}) D^2}{c_{\text{em}}} \right]^{(6+p)/(13+2p)} \left(\frac{\nu}{\nu_0} \right)^{-1}. \quad (59)$$

The velocity of the ejecta at the shock is then given by $V_{\text{shock}}(t_{\text{peak}}) = (n-3)/(n-2) R_s(t_{\text{peak}})/t_{\text{peak}}$. This velocity depends on the uncertain parameters f and especially ζ . However, this dependence is very weak. With $p=3$ one gets $R_s(t_{\text{peak}}) \propto (f\zeta)^{-1/19}$. For $\zeta = 10^{-3}$ the radius and velocity are only $\sim 30\%$ larger than for $\zeta = 1$.

Using Eq. (59), we can plot lines of constant shock velocity into a diagram with peak radio luminosity versus time of peak flux, *assuming* that SSA dominates (Fig. 6). Each SN can now be placed in this diagram to give a predicted shock velocity. If this is lower than the observed value (as measured by VLBI or from line profiles) SSA gives a too low flux and should therefore be relatively unimportant and free-

free absorption instead dominate. In Fig. 6 we show an updated version of the figure in [32]. The most interesting point is that most Type Ib/Ic like SNe 1983N, 1994I, 1998bw and 2002ap, fall into the high velocity category, while Type IIP, like SNe 1999em, 2004et and 2004dj, as well as the Type IIL SNe 1979C and 1980K, and the Type IIn SNe 1978K, 1988Z, 1998S fall in the free-free group. Strong, direct observational evidence for free-free absorption, however, only exist for SN 1979C and SN 1980K [149]. SN 1987A is clearly special with its low mass loss rate, but is most likely dominated by SSA [142, 135, 36].

Although the injected electron spectrum from the shock is likely to be a power law with $p_i \approx 2$ ($\alpha \approx 0.5$), the integrated electron spectrum is affected by synchrotron, Compton and Coulomb cooling. The column density of electrons with a Lorentz factor γ is

$$N(\gamma)s = \frac{U_{\text{rel}}(p-2)}{E_{\text{min}}^2} s(\gamma) \left(\frac{\gamma}{\gamma_{\text{min}}} \right)^{-p_i} \quad (60)$$

where $s(\gamma)$ is the effective thickness of the region of relativistic electrons, which depends on their energy. For energies where cooling is not important $s \approx V_s t/4$. For electrons with short cooling times, i.e., $t_{\text{cool}} \ll t$, one has instead $s(\gamma) \approx V_s t_{\text{cool}}(\gamma)/4$. Including all loss processes one can then write

$$N(\gamma)s \approx \frac{U_{\text{rel}}(p-2)}{E_{\text{min}}^2} \frac{V_s t}{4} \left(\frac{\gamma}{\gamma_{\text{min}}} \right)^{-p_i} \left[1 + \frac{t}{t_{\text{Coul}}(\gamma)} + \frac{t}{t_{\text{Comp}}(\gamma)} + \frac{t}{t_{\text{synch}}(\gamma)} \right]^{-1}. \quad (61)$$

Here t_{Coul} , t_{Comp} and t_{synch} are the Coulomb, Compton and synchrotron time scales, respectively. The expressions for t_{synch} are given by Eq. (40) and for t_{Comp} by Eq. (44).

The total number of relativistic electrons may either be assumed to be proportional to the total mass, if a fixed fraction of the shocked electrons are accelerated, or be proportional to the swept up thermal energy. In the first case, $U_{\text{rel}} \propto \dot{M}/u_w$, while in the second $U_{\text{rel}} \propto \dot{M}V_s^2/u_w$, so that in general $U_{\text{rel}} \propto \dot{M}V_s^{2\varepsilon}/u_w$, where $\varepsilon = 0$ or 1 in these two cases. If the magnetic field is in equipartition, as above, $B^2 \propto \rho V_s^2 \propto \dot{M}/t^2$ and using $V_s = (n-3)/(n-2)R_s/t \propto t^{-1/(n-2)}$, we find for the non-cooling case

$$F_V(\nu) \propto C_*^{(5+p)/4} t^{-(p-1)/2-(1+2\varepsilon)/(n-2)} \nu^{(1-p)/2}, \quad (62)$$

while for the synchrotron cooling case we instead get

$$F_V(\nu) \propto C_*^{(2+p)/4} t^{-(p-2)/2-(1+2\varepsilon)/(n-2)} \nu^{-p/2}. \quad (63)$$

The cooling case therefore steepens the spectrum by $1/2$, but flattens the light curves compared to the non-cooling case, for the same p . Inverse Compton losses have a similar effect. At low energy, Coulomb losses may be important, causing the electron spectrum to flatten. These complications are discussed in e.g., [69]. The main thing to note is, however, that the optically thin emission is expected to be sensitive

the shock. The secondary electrons are distinguished from the primary by being injected with a higher Lorentz factor than the primary, $\gamma \sim 68$. For proton-proton collisions to be important the effective optical depth for the high energy protons, $\sim 2.7(C_*/10^3)(V_s/5000 \text{ km s}^{-1})^{-2}(t/100 \text{ days})^{-1}$, has to be $\gtrsim 0.1$. Proton - proton collisions are therefore mainly important for shocks in very high density CS media, both for high energy gamma-ray and neutrino detections, but also as a source of electrons, giving rise to synchrotron emission in radio [112].

For a sufficiently dense CSM, $C_* \gtrsim 10^2$, and a high proton acceleration efficiency, $\gtrsim 10\%$, the neutrino flux in the GeV-PeV range may be detectable with IceCube out to a distance of 10–20 Mpc. There may also be the possibility of detecting GeV gamma-rays by Fermi in very long integrations (of the order of one year). The Cherenkov Telescope Array (CTA) will have more than an order of magnitude higher sensitivity in only 100 hours at TeV energies. Depending on the proton spectrum a strongly interacting SN may be detected out to 100 – 200 Mpc [113].

The typical frequency of the radio emission from the secondary electrons is in the range 3 – 3000 GHz [113], higher than the typical frequency of the primary electrons. The main problem for detecting the radio emission from these secondary electrons (and of course also the primary) is free-free absorption by the dense CSM (Eq. 49). However, for high frequencies, $\gtrsim 100$ GHz and large shock radii, $\gtrsim 10^{16}$ cm, i.e., late epochs, the CSM may be transparent for the radio photons, for parameters where the optical depth to the proton-proton collisions is large enough for significant secondary electron production. Detection of this emission would be highly interesting for understanding both the structure of collisionless shocks and cosmic ray acceleration in SNe.

6 Examples of circumstellar emission from different SN types.

As illustrations of the processes described above we discuss in this section a number of well observed SNe of different types. These should be seen as selected examples, but without any attempt of a complete list of references.

For later reference we show in Fig. 7 a compilation of light curves from a sample of SNe of different types. We note the large range, from bright Type II_{ns} to faint objects like SN 1987A. Radio light curves show a similar diversity.

6.1 Type IIP

Type IIP SNe are the most common class of supernovae, assumed to arise from 9 – 17 M_\odot red supergiant progenitors. In general, these have moderate mass loss rates $\dot{M} \sim 10^{-6} M_\odot \text{ yr}^{-1}$ and slow winds, $u_w = 10 - 20 \text{ km s}^{-1}$. Because of their comparatively low mass loss rates the X-ray emission is not very strong (Fig. 7). This is also the case for the radio emission and absorption effects are only seen very

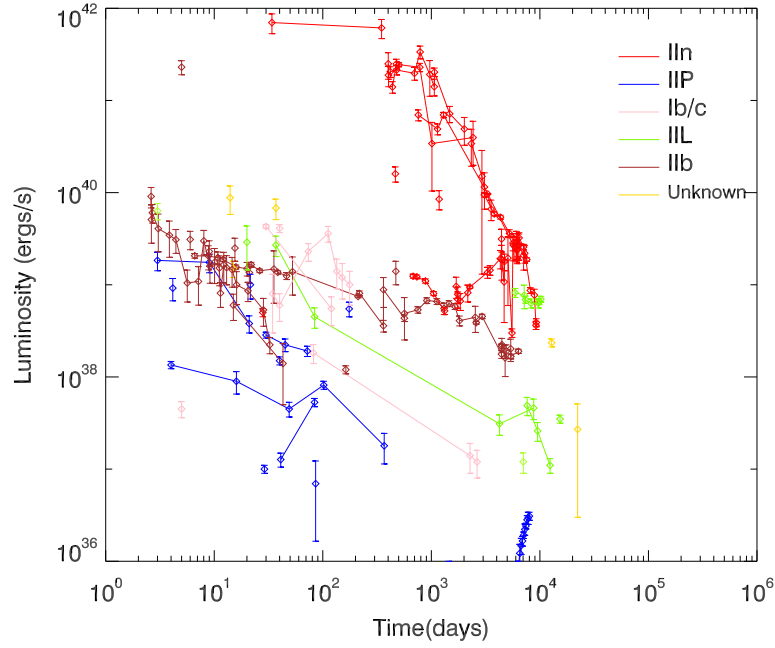


Fig. 7 Compilation of X-ray light curves of different types of supernovae. Note the large range, from faint objects, like SN 1987A (blue points coming up at ~ 5000 days), to the very bright Type II In SNe. With permission from [56].

early. Some of the best studied examples include SNe 1999em, 2004et and 2004dj [4, 10, 100].

In [41] the X-ray and radio observations were discussed for different assumptions about the efficiency for electron acceleration and magnetic field, ϵ_e and ϵ_B , and in Fig. 8 we show fits to the light curves of SN 2004et for different assumptions. For low magnetic fields, small ϵ_B , inverse Compton cooling by the photospheric emission was important for the relativistic electrons, while for a high ϵ_B synchrotron cooling was important. In both cases, the light curves were strongly affected by cooling during the first ~ 100 days. In the upper panel with a weak magnetic field the cooling of the relativistic electrons at early times is dominated by inverse Compton cooling by the optical radiation from the SN, resulting in a flat light curve. In the lower panel the situation is the opposite, with synchrotron cooling dominating early. The turn-on is caused by decreasing free-free absorption in both cases.

From the free-free absorption turn-on at ~ 20 days at 5 GHz, the mass loss rate was estimated to be $\dot{M} \approx 1 \times 10^{-5} (T_e/10^5 \text{ K})^{3/4} (u_w/10 \text{ km s}^{-1}) M_\odot \text{ yr}^{-1}$, again depending on the uncertain temperature of the CSM. Because of the extended red

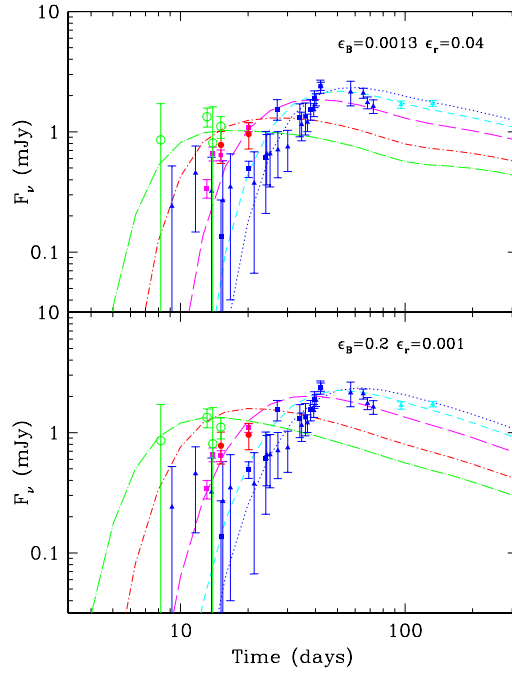


Fig. 8 Observed and model radio light curves (solid lines) of SN 2004et for different assumptions for the magnetic and relativistic electron energy densities, given in the figures. With permission from [41].

supergiant progenitor the CSM temperature may have been somewhat lower than for the Type IIL SNe in [93], i.e., $\lesssim 10^5$ K. The mass loss rate would then be similar to those of galactic red supergiants.

No boxy optical line profiles have been observed in optical spectra for a Type IIP SN, implying that the reverse shock in these cases is adiabatic, as is expected for the low mass loss rates.

6.2 Type IIL

The first well-observed radio SNe were the optically bright Type IIL SNe 1979C and 1980K [149]. Although observed with the new VLA immediately after explosion, SN 1979C was first detected only ~ 1 year after explosion at 5 GHz, while SN 1980K was first detected ~ 64 days after explosion [150, 149]. The wavelength dependent turn-on and sharp rise clearly showed that free-free absorption of a synchrotron spectrum could explain the observed light curves [30, 149, 93].

Modeling of the radio emission, including a calculation of the CSM ionization and temperature, is discussed in [93]. The deduced mass loss rates of SN 1979C and 1980K were $\sim 1 \times 10^{-4} M_{\odot} \text{ yr}^{-1}$ and $\sim 3 \times 10^{-5} M_{\odot} \text{ yr}^{-1}$, respectively, (assuming a wind velocity of 10 km s^{-1}). These high mass loss rates were the first indications that these SNe were not undergoing normal mass loss, characteristic of red supergiants, but more typical of a short-lived a super-wind phase.

There is also evidence for a periodic modulation of ~ 4.3 years of the radio light curve of SN 1979C, which has been interpreted as either pulsations of the progenitor or binary interaction by a massive companion in an eccentric orbit [151].

For SN 1979C VLBI observations have been possible up to 2005 [7, 96]. An analysis show an expansion of the radio shell that is close to free expansion.

Both SN 1979C and SN 1980k have been observed in the optical up to very recent epochs, now showing broad lines of especially [O I-III] [109]. It is therefore likely that they are now evolving into oxygen rich remnants, although the reverse shock has not yet reached the oxygen rich regions. The optical lines are instead likely to arise as a result of heating of the un-shocked interior by the X-rays from the reverse shock [38], as discussed in Sect. 4.3.2.

6.3 Type *I Ib*

The best radio observations of any SN were obtained for SN 1993J. This SN was observed from the very beginning until more than a decade after explosion with the VLA at wavelengths between $1.3 - 90 \text{ cm}$ [146, 152], producing a set of beautiful light curves. In addition, the SN was observed with VLBI by two groups up to at least 16.9 years after explosion at 1.7 GHz [12, 95, 11, and references therein], resulting in an impressive sequence of images in which the radio emitting plasma could be directly observed (Fig. 9). These images showed a remarkable degree of symmetry and clearly resolved the shell of emitting electrons. The evolution of the radius of the radio emitting shell could be well fitted by $R_s \propto t^{0.86}$, implying a deceleration of the shock front, although there has been some discussion of the exact value of the exponent.

From a fit of the observed spectra for the different epochs the magnetic field and number of relativistic electrons could be determined for each epoch, as described in Sect. 5.4 and in [69]. Both these parameters showed a remarkably smooth evolution, with $B \approx 6.4(R_s/10^{16} \text{ cm})^{-1} \text{ G}$, and $n_{\text{rel}} \propto \rho V^2 \propto t^{-2}$. The magnetic field was close to equipartition, $B^2/8\pi \approx 0.14 \rho V_s^2$, i.e., $\epsilon_B \approx 0.14$, orders of magnitude higher than expected if the circumstellar magnetic field, of the order of a few mG, was just compressed, and strongly argues for field amplification, similar to what was discussed in Sect. 5.1. The energy density of relativistic electrons was, however, found to be much lower, $\epsilon_e \sim 5 \times 10^{-4}$. Contrary to earlier, simplified models for SN 1993J based on free-free absorption only [76, 146], the circumstellar density in these consistent models was found to have a $\rho \propto r^{-2}$ profile.

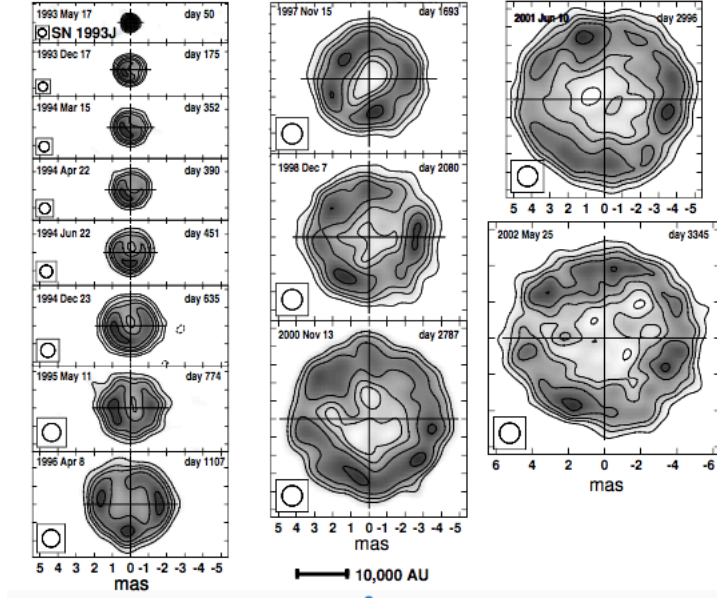


Fig. 9 Sequence of VLBI images of SN 1993J at 8.4 GHz between 50 to 3335 days after explosion. With permission from [6].

The high values of B implied that synchrotron cooling was important throughout most of the evolution for the electrons responsible for the cm emission, and also for the 21 cm emission before ~ 100 days. At early epochs, Coulomb losses were important for the low energy electrons. The injected electron spectrum was best fit with $p_i = 2.1$.

In Fig. 10, we show the excellent fit of the resulting light curves (see also [101]). The form of the light curves can be understood if, for simplicity, we assume equipartition, so that $B^2/8\pi \propto \rho V_s^2$. With $\rho \propto C_* R_s^{-2}$ and $V_s \propto R_s/t$, we find that $B \propto C_*^{1/2} t^{-1}$. The optically thick part is given by Eq. (57), so

$$F_\nu(\nu) \propto R_s^2 \nu^{5/2} B^{-1/2} \propto C_*^{-1/4} \nu^{5/2} t^{(5n-14)/2(n-2)}, \quad (64)$$

since $R_s \propto t^{(n-3)/(n-2)}$. For large n , we get $F_\nu(\nu) \propto t^{5/2}$. An additional curvature of the spectrum is produced by free-free absorption in the wind, $\propto \exp(-\tau_{\text{ff}})$, although this only affects the spectrum at early epochs. The time dependence of the optically thin part is given by Eq. (63).

Although the discussion above assumes a spherically symmetric CSM there could well be irregularities and clumping in the CSM. Chugai & Belous [49] propose a model in which the absorption is by clumps. The narrow line optical emission implies the presence of clumps, but they are different from those required for the radio absorption. The possible presence of clumps and irregularities introduces

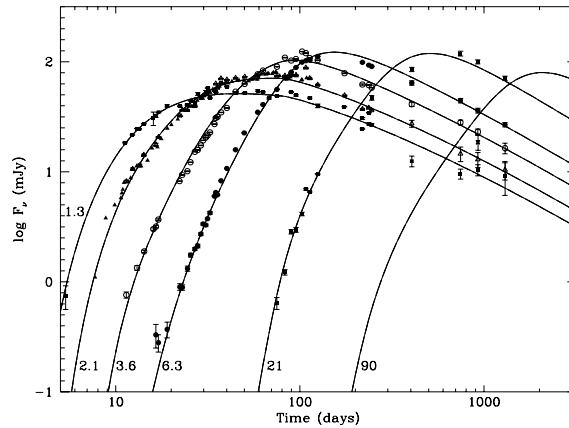


Fig. 10 Observed (dots) [146] and model radio light curves (solid lines) of SN 1993J. With permission from [69].

uncertainties into models for the radio emission, although rough estimates of the circumstellar density can still be obtained [14].

SN 1993J also has the most extensive set of observations in the X-ray band with essentially all existing X-ray satellites. OSSE on board the Compton Observatory detected the SN in the hard 50-150 keV energy band on day 12 and 30 with an X-ray luminosity of $\sim 5 \times 10^{40}$ erg s $^{-1}$ on day 12 [91]. However, by day 108 the 50-150 keV emission had already faded below their detection limit. This is one of the very few hard X-ray observations of any SN. A fit to the spectrum gave a temperature of 82_{-29}^{+61} keV.

ROSAT observed the SN in the 0.3-8 keV band from day 6 up to day 1800, summarised in [157]. From the observations up to ~ 50 days only a lower limit to the temperature of > 17 keV could be obtained, consistent with the OSSE observation. However, when it was re-observed at ~ 200 days the spectrum had changed dramatically to a soft spectrum with $kT < 2$ keV. The ROSAT observations, together with additional ASCA, Chandra, Swift and XMM observations, have revealed a continued softening of the spectrum, as illustrated by the slower luminosity decline in the 0.3 – 2.4 keV band compared to the harder 2 – 8 keV band, shown in Fig. 11 where all observations below 10 keV are summarised [26].

The transition from a hard to a soft X-ray spectrum can naturally be explained in the reverse - forward shock scenario discussed in Sect. 3.2. At early epochs the column density of the cool, dense shell between the reverse and forward shocks is very large and X-rays from the reverse shock cannot penetrate the shell. Consequently, the emission is dominated by the hard flux from the forward shock. At later epochs the soft spectrum from the reverse shock penetrates the cool shell as the column density decreases, and the line dominated emission from the cooling gas dominates.

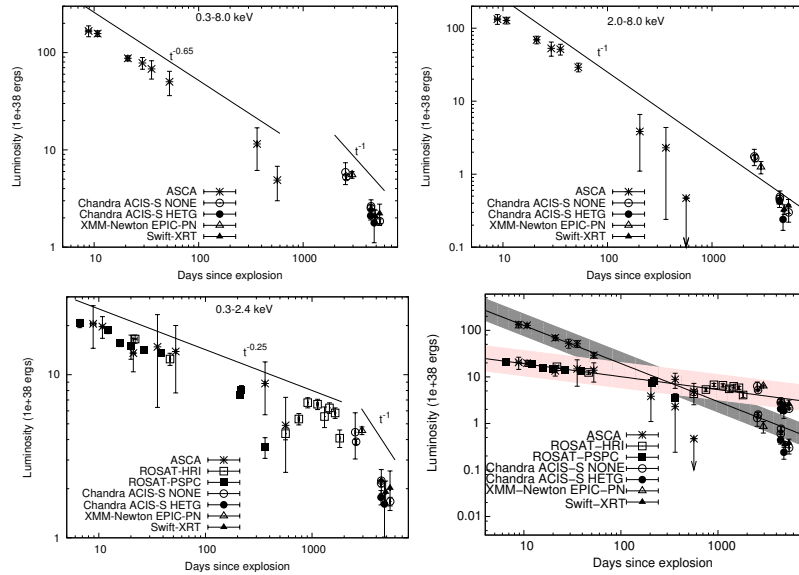


Fig. 11 Compilation of X-ray light curves of SN 1993J in different energy bands. Note the slower decay rate in the soft 0.3 – 2.4 keV band compared to the harder 2 – 8 keV band. With permission from [26].

As an illustration, we show in Fig. 12 the calculated X-ray spectrum at 10 days and at 200 days for SN 1993J [76]. At the first epoch the spectrum is dominated by the very hard spectrum from the circumstellar shock, which reaches out to $\gtrsim 100$ keV. The soft X-ray band is also dominated by the forward shock at this epoch. However, at 200 days the cool, dense shell has become partly transparent and the soft spectrum from the line dominated emission from the cooling gas behind the reverse shock now dominates. This evolution can also be seen in the light curves.

Nomoto & Suzuki [118] modeled the X-ray light curve during the first ~ 1000 days with a similar scenario, but invoked clumping in the cool shell to explain the fact that soft X-rays were observed also at early epochs. Clumping is a natural consequence of the Rayleigh-Taylor instabilities expected in the decelerating, radiative shell [27]. The full evolution up to ~ 15 years after the explosion has been analyzed and modeled in [26], who find that the reverse shock is likely to have been radiative up to ~ 5 years after explosion and adiabatic after that. This is consistent with the modelling in [119], who modeled the 8 year XMM spectrum, requiring a mix of radiative and adiabatic shocks. As discussed in Sect. 3.2, the time of the end of the radiative phase depends sensitively on both the composition and the structure of the ejecta.

A clear signature of the cool, dense shell, and therefore a radiative reverse shock, is the presence of broad, box-shaped line profiles, see in $H\alpha$ and other lines after ~ 1 year, and present to at least 2500 days after explosion [103, 71].

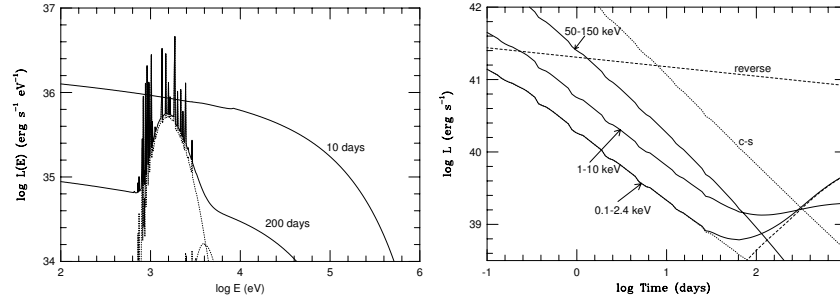


Fig. 12 left: Model X-ray spectra of SN 1993J at 10 days and at 200 days. At 10 days the free-free emission from the outer shock dominates, while at 200 days the cool shell is transparent enough for the line dominated spectrum from the reverse shock to dominate instead. Right: The solid lines give the luminosity in the 0.1-2.4, 1-10, and 50-100 keV bands, corrected for absorption, as a function of time, while the dotted lines give the total emitted luminosity from the reverse and circumstellar shocks. With permission from [76].

6.4 Type II_n

Type II_n SNe probably originate from a wide range of progenitors. The main defining characteristic is the presence of narrow H and He lines originating in a dense CSM. The broad wings are a result of electron scattering [47]. Using these to estimate the expansion velocity of the ejecta can therefore be highly misleading. Instead, the line profile results from a random walk in frequency for each scattering. The thermal velocity of the electrons is $V_{\text{therm}} = 674(T_e/10^4 \text{ K})^{1/2} \text{ km s}^{-1}$ and the number of scatterings, $N \approx \tau_e^2$. The FWHM of the line will therefore be $\sim N^{1/2}V_{\text{therm}} \approx 674 \tau_e (T_e/10^4 \text{ K})^{1/2} \text{ km s}^{-1}$. For a FWHM $\sim 2000 \text{ km s}^{-1}$, as observed in e.g., SN 2010jl [73], one needs $\tau_e \gtrsim 3$ if $T_e \sim 10^4 \text{ K}$.

The duration of this phase ranges from a few days, or weeks, like SN 1998S [61] and SN 1995N [72], to many years like SN 2010jl [73]. The former have a fast decline of the optical luminosity, while the latter have broad light curves, lasting for a year or more. The integrated luminosity is consequently an order of magnitude higher for the SN 2010jl-like events. This suggests that these SNe may originate from two different classes of progenitors and it has been suggested that the SN 1998S-like SNe come from RSGs with enhanced mass loss rates, $\sim 10^{-4} M_{\odot} \text{ yr}^{-1}$ [72], like the super-wind of VY CMa, while the more long-lasting come from LBV progenitors, with episodic mass loss rates of $\sim 0.1 M_{\odot} \text{ yr}^{-1}$. This is also consistent with their different host environments [144], where the SN 1998S-like have metallicities similar to the Type IIP SNe, while the SN 2010jl-like have lower metallicities similar to the SN imposters. From a study of X-ray emission, Dwarkadas & Gruszko [57] found that many supernovae, especially those of Type II_n, appear not to be expanding into a steady wind region.

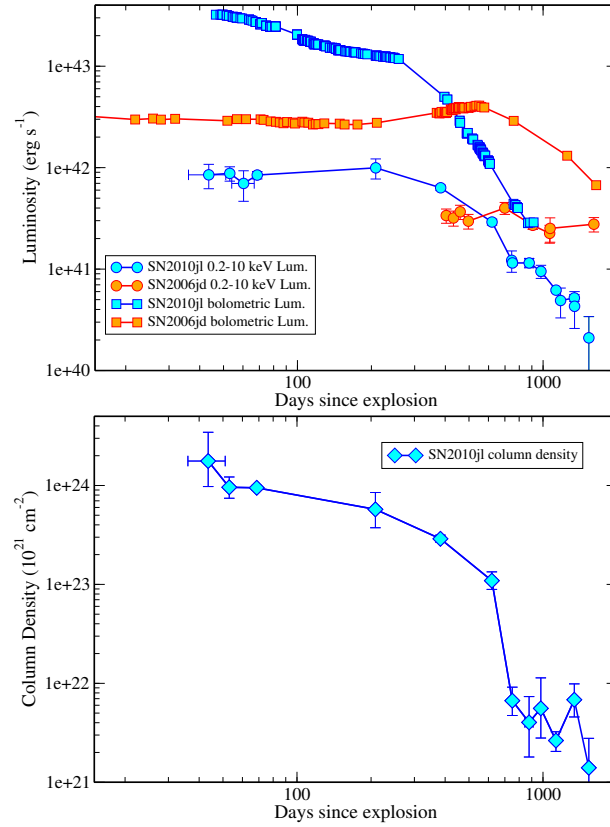


Fig. 13 Upper panel: Evolution of the 0.2-10 keV X-ray luminosity of the Type II SNe 2010jl and 2006jd (orange) together with the optical-NIR bolometric luminosity (blue). Lower panel: Evolution of the column density for SN 2010jl. Note the decrease of the initially very large column density caused by the expansion of the ejecta. With permission from [25].

These long lasting, and therefore more energetic SNe, belong to the most luminous SNe in the optical, radio and X-ray bands, including objects like SN 1988Z [3, 60, 154], and the well-observed SN 2010jl [73, 156, 122, 25]. The latter had an optical luminosity close to the superluminous Type II SNe. Fig. 13 shows the bolometric light curve from the optical/NIR from [73], together with the X-ray luminosity of SN 2010jl, as well as another luminous Type II, SN 2006jd [143]. Importantly, it was also observed with NuStar, resulting in an X-ray temperature of ~ 18 keV [122]. Although very luminous, the initial X-ray luminosity of SN 2010jl is an order of magnitude lower compared to the optical luminosity [122, 25]. Later this ratio increases and after ~ 1 year the X-ray luminosity dominates.

Equally interesting is the evolution of the X-ray column density, N , shown in the right panel of Fig. 13. At the first observation at ~ 40 days this was very high $N \sim 10^{24}$ cm⁻², but decreased with time. This may naturally be interpreted as a

result of the decreasing column density as the ejecta are expanding. For a wind one expects a $N \propto t^{-1}$ decrease (Eq. 17), while a shell may give a faster decrease.

Although very high, the X-ray column density was lower than that needed in order to explain the electron scattering profiles, which were seen up to ~ 1000 days and require an optical depth of $\tau_e \gtrsim 3$, corresponding to a column density of $\gtrsim 10^{25} \text{ cm}^{-2}$. These two constraints are difficult to combine in a spherically symmetric model. In [73] it is instead proposed that, based on the hydrodynamical calculations by van Marle et al. [147], which preceded SN 2010jl, the SN ejecta are expanding in a dense bipolar CSM, similar to that of Eta Car [136]. In this case, the density and column density are considerably higher in the polar directions than in the equatorial direction, presumably due to mass loss from a fast rotating star. In this case von Zeipel's theorem implies that the strongest mass loss will occur from the poles.

A SN exploding inside such a CSM would then have a shock velocity higher in the equatorial regions, $V_s \propto (\dot{M}/u_w)^{-1/(n-2)}$ (Eqs. 7 and 8), and also deposit more of its energy in this direction. The shock would therefore first break through the shell in the equatorial direction, where the X-ray (and radio) emission would first be seen. It would then still be deep inside the CS shell at high latitudes, where most of the emission is released as X-rays, which are then thermalized into optical radiation, resulting in a luminosity according to Eq. (21).

In radio, SN 2010jl was first detected on day ~ 700 [25], which is typical of these bright SNe, indicating that free-free absorption by a dense CSM absorbed the radio emission at earlier phases, consistent with a large mass loss rate parameter.

High resolution optical spectra of SN 2010jl, as well as other IIn (e.g., [143]), showed narrow lines with velocity $100 - 1000 \text{ km s}^{-1}$, which is in the range observed for the CSM from an LBV progenitor. From the state of ionisation, as well as from nebular diagnostics, the density of this component was inferred to correspond to a mass loss rate of $\sim 10^{-3} M_\odot \text{ yr}^{-1}$, much lower than that needed to explain the large continuum flux. These two components resemble those also seen in Eta Car.

Several of these bright Type IIn SNe have been followed for several decades. An interesting example is SN 1978K [89], where a high resolution spectrum from 2014 shows optical lines with a FWHM $\lesssim 600 \text{ km s}^{-1}$. This spectrum has hardly changed during 20 years, and shows that the SN is still interacting with the CSM. Kuncarayakti et al. [89] compare this spectrum to that of the ring of SN 1987A [77] and find striking similarities, both with respect to line widths and degree of ionization. In both cases, the latter spans a range from neutral, like $\text{H}\alpha$ and $[\text{O I}]$ up to $[\text{Fe XIV}]$. In the case of SN 1987A we know that these lines arise as a result of radiative shocks propagating into dense clumps in the ring, and Kuncarayakti et al. speculate that a similar geometry may be present in SN 1978K, in spite of the symmetric lines.

UV lines of C III], C IV, N III], N IV] and O III] are useful as abundance indicators and there are for several Type III and Type IIn, including SNe 1979C, 1995N, 1998S and 2010jl, strong evidence for CNO processing from lines in the circumstellar medium [68, 71, 72, 73]. This provides independent evidence for strong mass loss from the progenitor.

The Type II_n SN 1986J has been followed in both radio, optical and X-rays. The VLBI imaging is especially interesting since it gives a spatially resolved view of the interaction (e.g., [13, 128]). These images show a highly non-spherical structure with a number of 'protrusions', indicating interaction with large scale clumps. The average expansion velocity measured between 1999 and 2008 was $5700 \pm 1000 \text{ km s}^{-1}$, considerably higher than in the optical at the same epochs [110], where the emission was probably mainly coming from the ionized oxygen emitting core of the SN. Up to ~ 2002 the VLBI structure was dominated by one big blob off-center. At the same time as this decayed a new central blob appeared with increasing flux, showing a free-free absorbed spectrum with a decreasing optical depth. Bietenholz et al. [13] propose that this may either be the result of the emission from a compact object, explaining the central position, or as a result of the interaction of a large scale cloud which happens to be in the line of sight to the centre. An alternative interpretation is that the central emission is the result of circumstellar interaction with the inner boundary of a dense disk resulting from common envelope interaction of the progenitor [34]. The continued evolution of the radio structure is of obvious interest.

Chugai [46] has proposed that the X-ray emission from SN 1986J is the result of the forward shock front moving into clumps, as opposed to the reverse shock emission. One way to distinguish these cases is by the width of line emission; emission from the reverse shock wave is expected to be broad. It has not yet been possible to carry through with this test [82].

6.5 SN 1987A

Recent developments in connection to both the ejecta and the ring interaction are reviewed in [107], including full references to the literature. We therefore limit ourselves to some general remarks of interest for CS interaction.

Because of its distance SN 1987A is unique in that one can resolve the CS environment around the SN. The most apparent structure of the CSM is the ring system, consisting of the equatorial ring at a distance of $\sim 6 \times 10^{17} \text{ cm}$ and the outer rings at $\sim 2 \times 10^{18} \text{ cm}$. One can therefore study the different regions of the interaction in detail. Although the CSM structure of SN 1987A probably is not typical to the majority of core collapse SNe, the fact that we can study it resolved, and also time dependent, means we can learn a great deal from a study of it in the different wavelength domains.

In Fig. 14 we show the evolution of the flux from the ring and the general CSM interaction in different wavelength ranges, which reflect the structure of the CSM. Initially SN 1987A was extremely faint in both radio and X-rays, consistent with the low mass loss rate, $\sim 10^{-7} M_{\odot} \text{ yr}^{-1}$, and high wind velocity, $\sim 450 \text{ km s}^{-1}$, associated with the B3Ia progenitor star [36]. At ~ 1200 days the radio flux, however, increased rapidly and has since day ~ 2000 increased almost exponentially [155]. At about the same time as the radio increased also X-rays were observed and fol-

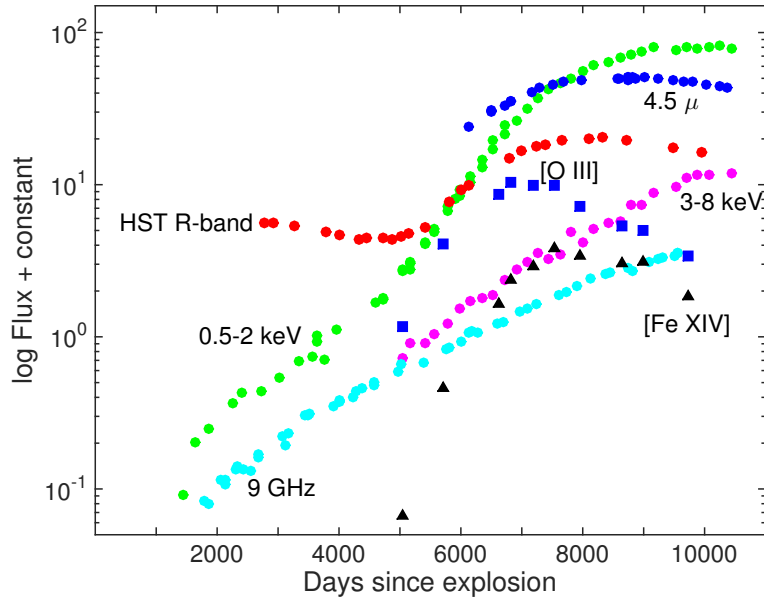


Fig. 14 Compilation of light curves in different wavelength bands and lines from the ring of SN 1987A. For clarity the different band and lines are arbitrarily scaled in flux. The HST R-band (red dots), [O III] 5007 Å (blue squares) and [Fe XIV] 5303 Å (black triangles) points are from [74]. The Chandra and ROSAT 0.5 - 2 keV (green dots) and 3 - 8 keV (magenta dots) points are from [65] and [80], the IRAC 4.5 μm (blue dots) points from [2] and the ATCA 9 GHz (cyan dots) from [117].

lowed the evolution of the radio emission up to day ~ 4500 . After the impact with the ring the soft X-rays increased even faster up to ~ 7000 days [80], after which it has levelled off [65]. The pre-impact evolution was explained as a result of the interaction of the nearly freely expanding ejecta with the photoionized H II region, formed by the progenitor, having a nearly constant density, $\sim 100 \text{ cm}^{-3}$ [36]. As the decelerating ejecta started to interact with the clumps forming the CS ring, an increasing number of hotspots became visible in the optical, while at the same time the soft X-ray flux increased at the same rate.

At ~ 7000 days the optical flux reached a peak, and has since decreased, while new spots have appeared outside of the ring [74]. This evolution is seen most clearly for the different high ionization lines, like the [O III] 5007 Å and [Fe XIV] 5303 Å lines formed in the cooling gas behind the shocks (Fig. 14). The mid-IR shock heated dust emission [2] has also reached a peak, while the X-ray emission has levelled off [65]. The hard X-rays and the radio emission are continuing to rise [65, 155].

The basic scenario for this interaction, once the collision with the clumps in the ring started, is that of a forward shock propagating into the clumps, while the pressure behind the shock sends a reflected shock back into the ejecta which gives

rise to a reverse shock. Because the density of the clumps is $\gtrsim 10^4 \text{ cm}^{-3}$, while the ejecta density close to the shock is only $\sim 10^2 \text{ cm}^{-3}$ the velocity of the forward shock will be a factor $\sim (\rho_{\text{clump}}/\rho_{\text{ej}})^{1/2} \approx 10$ lower than the forward shock (Eq. 23). From the expansion seen in the X-ray and radio images the velocity of the forward shock is $2000 - 4000 \text{ km s}^{-1}$, giving a shock velocity into the clumps of $\sim 200 - 500 \text{ km s}^{-1}$.

The difference between the evolution of the optical and mid-IR light curves on the one hand and the X-ray and radio on the other can be understood since the optical and dust emission are only coming from the shocked clumps in the ring; the X-ray and radio emission have a major contribution from lower density regions between the clumps as well as above and below the ring plane. The SN ejecta are now starting to probe the region outside the ring, which will provide insight into the mass loss history of the progenitor.

The interaction of the SN ejecta and the CSM in SN 1987A is a nearly perfect shock laboratory, and are useful for understanding both the thermal and non-thermal processes discussed earlier in this review. From the radio [155] and hard X-rays [65] one can study the acceleration of relativistic particles at the reverse shock, in both time and space. The optical (e.g., [78]) and soft X-rays (e.g., [54]) in contrast give information about the thermal processes from the shocks propagating into the dense clumps in the ring, while the harder X-rays mainly come from non-radiative higher velocity shocks.

From the optical line widths of the hotspots one finds velocities between $200 - 700 \text{ km s}^{-1}$. It is therefore clear that these lines are shock excited, in contrast to direct photoionization, which would give lines with $\text{FWHM} \sim 10 \text{ km s}^{-1}$. For $T_e \lesssim 2.6 \times 10^7 \text{ K}$ line emission dominates the cooling rate, so $\Lambda(T_e) \approx 2.4 \times 10^{-23} (T_e/10^7 \text{ K})^{-0.48} \text{ erg s}^{-1} \text{ cm}^3$, and with the shock condition for T_e , the cooling time behind the shocks propagating into the dense clumps becomes

$$t_{\text{cool}} = 38 \left(\frac{V_s}{500 \text{ km s}^{-1}} \right)^{3.4} \left(\frac{n_e}{10^4 \text{ cm}^{-3}} \right)^{-1} \text{ years.} \quad (65)$$

where n_e is the pre-shock electron density. The presence of lines with a velocity $\sim 700 \text{ km s}^{-1} \sim 15$ years after the impact therefore implies a pre-shock density of $\gtrsim 4 \times 10^4 \text{ cm}^{-3}$, in agreement with the highest densities determined from the unshocked ring [94]. These shocks belong to the highest velocity radiative shocks we know of.

Shocks with higher velocity do not cool and are only seen in X-rays, with the exception of some coronal lines, like the [Fe XIV] line shown in Fig. 14. This applies to the outward propagating blast wave between the clumps, as well as below and above the ring plane, which now expands with a velocity of $\sim 1854 \text{ km s}^{-1}$ [65]. It is also the case for the reflected and reverse shocks moving back into the ejecta. The X-ray emission is therefore the sum of all these different components.

The maximum ejecta velocity seen from the broad $\text{H}\alpha$ component is $\sim 11,000 \text{ km s}^{-1}$. This emission is coming from the region close to the reverse shock, where neutral H atoms are excited and ionized by the hot gas behind the reverse shock. From the

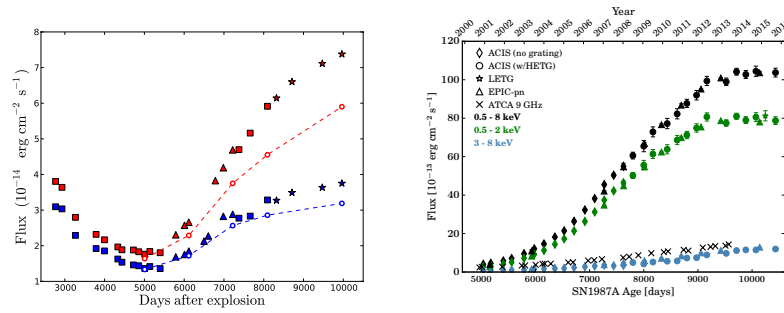


Fig. 15 Optical R (red) and B (blue) band light curves of the ejecta (left) (update of [90]) and X-rays (right) of SN 1987A, with permission from [65].

radio and X-rays the expansion velocity in the observer frame of the reverse shock has been estimated to $2000 - 4000 \text{ km s}^{-1}$. The reverse shock velocity is therefore $\sim 8000 \text{ km s}^{-1}$, and the emission is therefore expected mainly from hard X-rays. This is also the region where most of the acceleration of the relativistic electrons, responsible for the radio emission, takes place.

SN 1987A provides one of the best examples of the thermalization of the X-rays from the circumstellar interaction by the SN ejecta (Fig. 15). Up to day ~ 5000 the light curve of the ejecta was decaying with a rate consistent with that of the radioactive decay. However, after that it has increased by a factor 2–4 [90]. At the same time the morphology of the ejecta changed from centrally peaked to a horseshoe like shape.

This can easily be understood when we compare this light curve with the X-ray light curve in Fig. 15. Both the increase of the optical flux and the change in morphology can consistently be explained as a result of the X-ray deposition from the ring collision by the ejecta. The soft and hard X-rays can penetrate much of the H and He rich outer regions of the ejecta. At the boundary of the metal rich core the photoelectric opacity increase sharply and most of the X-rays are here deposited, giving rise to the limb brightened morphology [75]. We can therefore directly study the effects of the CSM interaction on the ejecta with spatial resolution.

The hydrodynamic interaction of the ejecta and the CSM of SN 1987A has been modeled by 3D hydrodynamic simulations by Potter et al. [130] and by Orlando et al. [123]. The former authors had an emphasis on the radio evolution, while the latter had their emphasis on the X-ray evolution. Both groups assume a CSM structure similar to that by Chevalier & Dwarkadas [36]. Because this structure was proposed to explain the early radio and X-ray evolution it is not surprising that they can explain the early evolution in these bands well.

The second phase is dominated by the interaction with the ring, which dominates the soft X-rays as well as the optical emission. From their high resolution AMR FLASH simulations Orlando et al. model the fragmentation of the clumps in the ring in considerable detail. This was already done for individual clumps in 2D with

high resolution by Borkowski et al. [19], although with a more simplified model for the ejecta and CSM. The main result of this is that the clumps are crushed by the radiative shock and shredded by the Richtmyer-Meshkov and Rayleigh-Taylor instabilities behind it.

In the final phase, beginning at ~ 32 years, the blast wave has propagated past the ring, while the reverse shock is propagating deep into the envelope of the SN. The X-ray emission is dominated by the ejecta and the morphology is characterized by shocked ejecta clumps. It is now becoming a more classical remnant. The fact that the optical, X-ray, mid-IR and radio fluxes are decreasing or leveling off, as discussed above, shows that we are now in this transition phase.

The radio evolution is complex, showing a varying spectral index, increasing rapidly from $\alpha \approx 0.75$ on day 1200 (the impact at the termination shock of the BSG wind) to $\alpha \approx 1.0$ on day 2400 after which it decreased linearly to $\alpha \approx 0.7$ on day 8000 [155]. Another interesting aspect is the east – west asymmetry of the radio emission. In contrast to the X-rays, the radio intensity is strongest on the eastern side, which is also where the expansion velocity measured from the radio images is considerably faster ($\sim 6000 \text{ km s}^{-1}$) than on the western side ($\sim 1900 \text{ km s}^{-1}$). From the relation $B \propto V_s^{1.5}$, predicted by the Bell instability [8], Potter et al. [130] argue that the higher intensity on the eastern side is a direct consequence of the stronger magnetic field there, which in turn is a consequence of the higher expansion velocity in this direction. The latter may be a result of an anisotropic explosion geometry in the ejecta.

There are several things we can learn from these observations, relevant to the observations of more distant SNe. The most important is perhaps that the CSM around the SN progenitor can be very complex, reflecting the evolution of the progenitor star. The simple spherically symmetric structure most often assumed in more distant unresolved SNe, may sometimes be a poor approximation. This applies to both the CSM and the SN ejecta, which in the case of SN 1987A are both highly asymmetric. In addition, SN 1987A shows that even if no CS interaction is seen at early times, it may become important after several years, depending on structures at large distances from the SN. In this respect it is interesting to compare with the late optical, radio and X-ray turn-on for the Type Ib/c SNe (Sect. 6.6)

There are also other aspects of SN 1987A which are seen in other SNe. E.g., the coronal lines which are seen in Type IIIn and Ibn SNe are also observed in spectra from the SN 1987A ring [79]. In SN 1987A these are clearly formed in the post-shock gas. For more distant SNe high resolution spectra are, however, needed to distinguish between shock excitation and photoionization by X-rays of unshocked gas. If shocked emission, one can then from Eq. (65) estimate the pre-shock density.

For the X-rays seen from shell interaction in Type Ib/c SNe (Sect. 6.6) or from a clumpy CSM one may have a similar situation to that of SN 1987A with several shock components contributing to the flux as from the blast wave and reverse shock in SN 1987A.

6.6 Type Ib/c

A review of radio and X-ray observations of Type Ibc SNe is presented in [33]. In general, these SNe have weaker radio and X-ray emission (Fig. 7) and a more gradual power law turn-on of their light curves compared to Type II SNe. The weaker emission is most likely a result of the higher wind velocities, $\gtrsim 1000 \text{ km s}^{-1}$, of the progenitor stars, thought to be Wolf-Rayet stars. The CSM density is therefore a factor of $\gtrsim 100$ lower compared to a red supergiant progenitor of the same mass loss rate.

The power law turn-on is typical for synchrotron-self-absorption, which well fits the light curves and spectra [41]. From the optically thin emission it is found that the spectral index in the radio in general is steeper than for other types of SNe, with $\alpha \approx 1$. Because of the low CSM density synchrotron cooling is not important at radio frequencies. At early times Compton cooling may be important as long as the bolometric luminosity is $\gtrsim 2 \times 10^{42} \text{ erg s}^{-1}$ [15], but becomes unimportant as the SN fades. The steep spectral index therefore implies a steep electron injection spectrum with $p \approx 3$, possibly a result of a cosmic ray dominated shock.

Because of the high shock velocity and low CSM density both the forward and reverse shocks are likely to be adiabatic, unless the reverse shock is propagating into a heavy element dominated core.

The best observed Type Ib/c in radio is SN 1994I observed by Weiler et al. with the VLA [148]. Originally classified as a Type Ic, the He I $\lambda 10830$ line was clearly detected in an early NIR spectrum with a maximum velocity $29,900 \text{ km s}^{-1}$ [63]. A review of radio and X-ray observations of Type Ibc SNe is presented in [33]. In Fig. 16 we show the radio light curves at different wavelengths from an analysis by [1], showing the gradual turn-on, and a steep decline after the peak, common to other Type Ib/c SNe.

Alexander et al. [1] found that these light curves could be well fitted with a SSA model, without any free-free absorption (solid line in Fig. 16). The mass loss was estimated to $\dot{M} \approx 10^{-5} M_{\odot} \text{ yr}^{-1}$ for a wind velocity of 1000 km s^{-1} , but depends on uncertain assumptions for ϵ_e and ϵ_B . The derived expansion velocity is less sensitive to these (Eq. 59) and was found to be $\sim 35,000 \text{ km s}^{-1}$, somewhat larger than that obtained from the optical, and typical of other Type Ib/c SNe (Fig. 6).

X-rays from SN 1994I were detected at an age of 6 - 7 years [84], although the identification has been challenged by [145]. This very late detection is difficult to explain either by thermal shock emission, inverse Compton or a single power-law synchrotron spectrum, extending from radio to X-rays. In [40] an explanation was suggested based on the broken power-law spectrum of the electrons in a cosmic ray dominated shock wave (Sect. 5.1), where the low energy electrons have a steeper spectrum than those at high energy, giving a high X-ray to radio ratio.

Although most Ib/c SNe are faint in radio and X-rays at early epochs, there are cases where strong emission in these bands has been observed to become bright on time scales of years. Examples of this are SN 2001em as well as the recent SN 2014C ([50] and [98, 111] and references therein). Both of these exhibited abrupt increases of the radio and X-ray flux at an age of ~ 700 days and ~ 150 days,

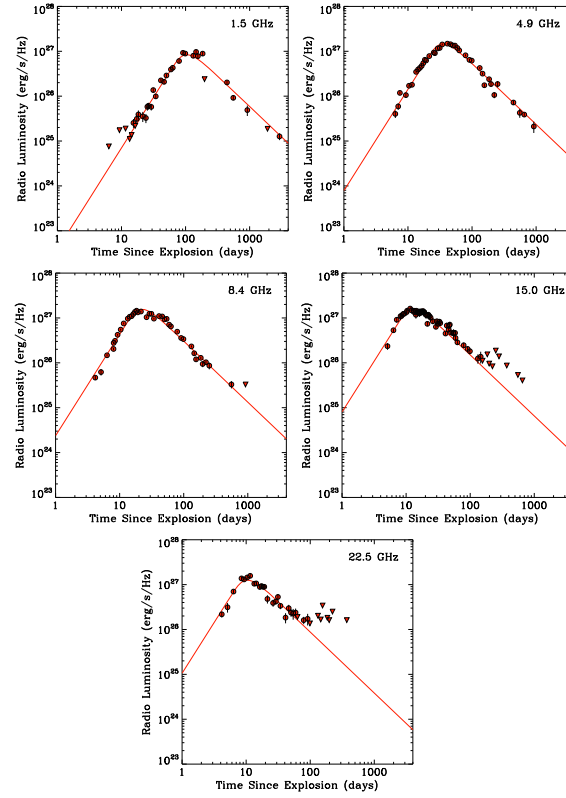


Fig. 16 Radio light curves of SN 1994I at different frequencies. Note the power law turn-on characteristic of synchrotron-self-absorption. The upside-down triangles mark upper limits. With permission from [1].

respectively (Fig. 17). At about the same time as the radio increase a strong, narrow $H\alpha$ line with FWHM $\sim 1800 \text{ km s}^{-1}$ was seen in SN 2001em.

In [50], the X-ray and radio evolution of SN 2001em was modeled by a He core with mass $\sim 2.5 M_{\odot}$ interacting with a massive H rich shell. The $H\alpha$ line was explained as a result of the accelerated, shocked shell, while the X-rays, assumed to have $kT_e \sim 80 \text{ keV}$, and radio came from the much faster reverse shock with a velocity of $\sim 5500 \text{ km s}^{-1}$. To yield the required velocity ratio of the shocked shell and reverse shock together with the observed X-ray luminosity a shell with mass $\sim 2 - 3 M_{\odot}$ at $\sim 6 \times 10^{16} \text{ cm}$ was required. Assuming a pre-shock velocity of $\sim 20 \text{ km s}^{-1}$ this shell may have been ejected $\sim (1 - 2) \times 10^3$ years before the explosion, and with a mass loss rate $\sim (2 - 10) \times 10^{-3} M_{\odot} \text{ yr}^{-1}$.

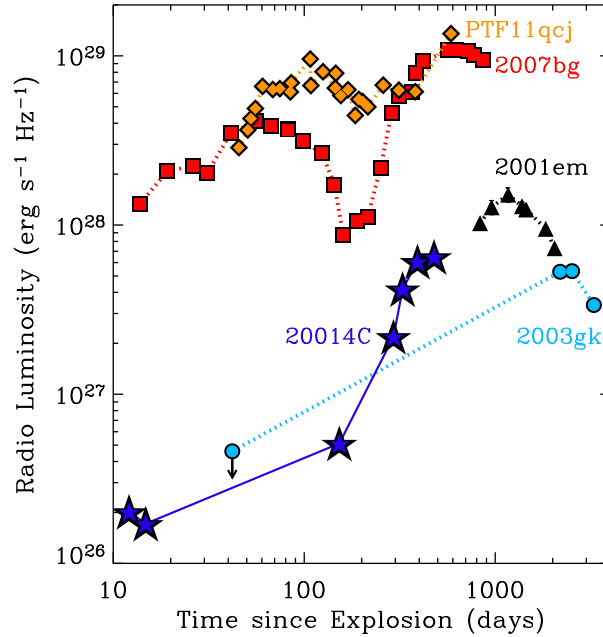


Fig. 17 Radio light curves at 7.1 - 8.5 GHz of the type Ib/c SNe 2001em, 2003gk, 2007bg, PTF11qcj and 2014C. With permission from [98].

The analysis of SN 2014C yielded a similar set of parameters [98]. However, NuSTAR observations of SN 2014C gave a well-determined temperature of ~ 18 keV, much lower than that assumed for SN 2001em. It is therefore likely that the temperature of SN 2001em was considerably lower than estimated above, and may possibly have come from the forward shock, illustrating the importance of hard X-ray observations. The thermal X-ray spectrum of SN 2014C also showed strong emission at 6.7-6.9 keV from He-like and H-like Fe K transitions, clearly demonstrating the thermal nature of the spectrum.

Several other Type Ic SNe show variability at radio wavelengths on time scales of weeks to months [153].

6.7 Type Ibn

While optical lines from the CSM are rare for Type Ib/c SNe, there exist a number of interesting cases where this has been observed, which are classified as Ibn, in analogy with the IIn. For a summary, see [127] and references therein.

The best studied object of this class is SN 2006jc. Early spectra displayed He I lines with a width extending to ~ 5000 km s $^{-1}$, which is low for a Ib SN, but similar

to Type II n lines [64]. The bluer He I lines had P-Cygni absorptions extending to $\sim 2000 \text{ km s}^{-1}$ with the minimum at $\sim 1000 \text{ km s}^{-1}$, typical of WR winds. An outburst of the progenitor was observed ~ 2 years before explosion [126]. The last spectra at ~ 175 days showed narrow lines with FWHM $\sim 1800 \text{ km s}^{-1}$, including H α .

SN 2006jc was detected with Swift and Chandra with a 0.5 - 10 keV luminosity of $(1 - 4) \times 10^{39} \text{ erg s}^{-1}$, peaking at ~ 110 days after which it decayed [83]. The Chandra spectrum displayed a very hard spectrum $dN/dE \propto E^{-0.24}$ [121]. No radio emission was detected. On day ~ 75 a strong red continuum excess appeared. At the same time the red wing of the initially symmetric He I lines faded. Both these aspects are indicative of dust formation [139], which was consistent with the observation of a strong NIR and mid-IR continuum from Spitzer [105].

Chugai [48] has modeled the optical and X-ray light curves, assuming a dense shell with a mass of $0.02 - 0.05 M_{\odot}$ within $\sim 2 \times 10^{15} \text{ cm}$, ejected one year before explosion. The dust formation is assumed to take place in the cool, dense shell behind the reverse shock, as was earlier proposed by Mattila et al., [105] based on Spitzer observations.

6.8 Relativistic expanding supernovae

There are a number of SNe Ic, SNe 1998bw, 2003lw, 2006aj, and 2009bb, that are inferred to have mildly relativistic expansion based on their high radio luminosity at an early time and a synchrotron self-absorption model. It is possible to estimate the minimum energy in the synchrotron emitting gas from the synchrotron luminosity and it is surprisingly high for ejecta accelerated in a normal supernova. In three of these cases (SNe 1998bw, 2003lw, 2006aj), there is a low luminosity gamma-ray burst (GRB) associated with the supernova, opening the possibility that the energetic emission is associated with a collimated flow from a central engine. However, Nakar & Sari [116] found that the basic properties of these events could be explained by a relativistic shock breakout model, but the required supernova energy is very large. In a revised model for SN 2006aj (GRB 060218), Nakar [115] suggested that a normal GRB jet was slowed and deposited its energy in an extended envelope around the progenitor star. The deposition of the jet energy, about 10^{51} ergs, into a small amount of mass gives an energetic shock breakout event, as observed. The radio emission from SN 2006aj can then be explained by the interaction of the supernova ejecta with a circumstellar wind [5].

6.9 Type Ia

Except for objects with very dense interaction like SN 2006gy, essentially all types of core collapse supernovae have shown radio and X-ray emission from circumstel-

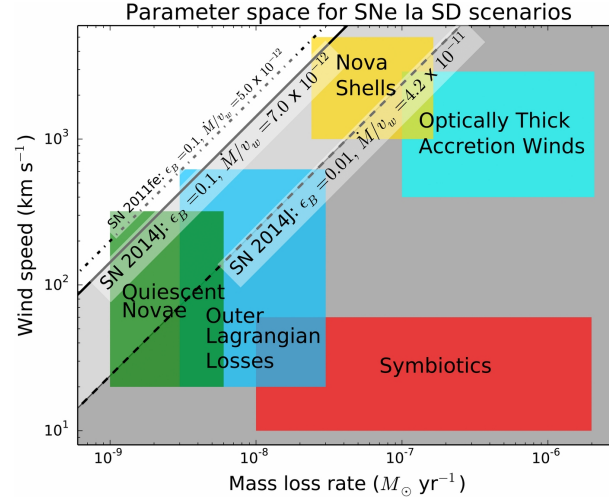


Fig. 18 Constraints on Type Ia single degenerate progenitors from radio observations of SN 2014J and SN 2011fe. Progenitors falling into the gray shaded areas should have been detected by the observations, and therefore are ruled out. With permission from [129].

lar interaction. On the other hand, Type Ia supernovae have not been detected as radio and X-ray sources. In some cases, this may be due to absorption by a very dense circumstellar medium. The Type IIn optical features in supernovae like SN 2002ic imply that a dense medium is present. It is possible in these cases that radio and X-ray emission is attenuated by absorption processes. However, the great majority of SNe Ia show no sign of circumstellar interaction at optical wavelengths and the low radio and X-ray emission is attributed to a low circumstellar density. The limits set on the surrounding density are more constraining than for other methods used for normal SNe Ia.

The occurrence of relatively nearby SNe Ia, e.g., SN 2011fe in M101 [45, 81] and SN 2014J in M82 [99, 129], has allowed especially strong limits on the radio and X-ray luminosities. Limits on the radio luminosity of individual events are in the range $10^{23} - 10^{24}$ ergs s⁻¹ Hz⁻¹. As can be seen in Fig. 6, the only core collapse supernova with a luminosity in this range is the early luminosity of SN 1987A. The X-ray limits of $\sim (4 - 7) \times 10^{36}$ erg s⁻¹ [99] are also lower than any core collapse SNe, with the exception of SN 1987A.

There are uncertainties in setting limits on the mass loss density because of the lack of a complete theory for particle acceleration and magnetic field amplification, i.e., values of ϵ_e and ϵ_B . With plausible assumptions on the efficiency of production of particles and fields, some proposed progenitors of SNe Ia can be ruled out, including ones where the companion star is a red giant (Fig. 18). Interaction with the interstellar medium easily produces emission below the observed limits, providing support for a double degenerate progenitor scenario. These limits, however, only

apply to the individual objects with good limits, and there may be other channels which apply to other objects.

7 Conclusions

During the last four decades, radio and X-ray observations have given us a new tool to study the CSM of different types of SNe. This has in turn yielded a completely new view of the evolution of the SN progenitors and the evolution during the last phases before the explosion. Mass loss has become the most important factor for understanding the different types of core collapse SNe.

Although there has been considerable progress in many respects, there remains much to be done. Here we list a few of the areas that need further study:

- A better understanding of the generation and efficiencies of magnetic field amplification and relativistic particle acceleration. These are crucial for deriving accurate mass loss rates from the radio observations.
- The importance of the geometry. Observations of supergiants in our Galaxy and of CS interaction give evidence for non-spherical CSM structure. SN 1987A is an obvious example, but there are many other indications that deviations from spherical geometry, as well as shell structures, are important.
- CSM interaction on timescales of years. We have been able to follow a few supernovae on long timescales, in some cases revealing the presence of shells and other structure. A more systematic monitoring of older supernovae would give important insight to the mass loss history preceding the final stage.
- The understanding of the mass loss mechanisms in the final stages before explosion. Although there are many proposals, there is no consensus as to what causes the strong mass loss in the final stages as observed in particular cases.
- Effects of binary evolution. Common envelope evolution and the related mass loss are clearly important. This process is expected to lead to an asymmetric distribution of the gas, possibly as a toroidal structure in the orbital plane. The structure of the ring of SN 1987A is an important lesson.

Acknowledgements RAC's research was partly supported by NASA grant NNX12AF90G, while that of CF by the Swedish Research Council.

Cross-References

- The Physics of Supernova 1987A
- Shock breakout theory.
- The Supernova - Supernova Remnant Connection
- Interacting Supernovae: Types IIIn and Ibn
- Interacting Supernovae and the Influence on Spectra and Light Curves

References

1. Alexander, K.D., Soderberg, A.M., Chomiuk, L.B.: A New Model for the Radio Emission from SN 1994I and an Associated Search for Radio Transients in M51. *ApJ* **806**, 106 (2015). DOI 10.1088/0004-637X/806/1/106
2. Arendt, R.G., Dwek, E., Bouchet, P., Danziger, I.J., Frank, K.A., Gehrz, R.D., Park, S., Woodward, C.E.: Infrared Continuum and Line Evolution of the Equatorial Ring around SN 1987A. *AJ* **151**, 62 (2016). DOI 10.3847/0004-6256/151/3/62
3. Aretxaga, I., Benetti, S., Terlevich, R.J., Fabian, A.C., Cappellaro, E., Turatto, M., della Valle, M.: SN 1988Z: spectro-photometric catalogue and energy estimates*. *MNRAS* **309**, 343–354 (1999). DOI 10.1046/j.1365-8711.1999.02830.x
4. Argo, M.K., Beswick, R.J., Muxlow, T.W.B., Pedlar, A., Fenech, D., Thrall, H.: MERLIN monitoring of recent core-collapse supernovae. *MmSAI* **76**, 565 (2005)
5. Barniol Duran, R., Nakar, E., Piran, T., Sari, R.: The afterglow of a relativistic shock breakout and low-luminosity GRBs. *MNRAS* **448**, 417–428 (2015). DOI 10.1093/mnras/stv011
6. Bartel, N.: Supernova VLBI. In: Y. Hagiwara, E. Fomalont, M. Tsuboi, M. Yasuhiro (eds.) *Approaching Micro-Arcsecond Resolution with VSOP-2: Astrophysics and Technologies, Astronomical Society of the Pacific Conference Series*, vol. 402, p. 243 (2009)
7. Bartel, N., Bietenholz, M.F.: SN 1979C VLBI: 22 Years of Almost Free Expansion. *ApJ* **591**, 301–315 (2003). DOI 10.1086/375267
8. Bell, A.R.: Turbulent amplification of magnetic field and diffusive shock acceleration of cosmic rays. *MNRAS* **353**, 550–558 (2004). DOI 10.1111/j.1365-2966.2004.08097.x
9. Bell, A.R., Lucek, S.G.: Cosmic ray acceleration to very high energy through the non-linear amplification by cosmic rays of the seed magnetic field. *MNRAS* **321**, 433–438 (2001). DOI 10.1046/j.1365-8711.2001.04063.x
10. Beswick, R.J., Muxlow, T.W.B., Argo, M.K., Pedlar, A., Marcaide, J.M., Wills, K.A.: Monitoring of the Prompt Radio Emission from the Unusual Supernova SN 2004dj in NGC 2403. *ApJL* **623**, L21–L24 (2005). DOI 10.1086/430049
11. Bietenholz, M., Bartel, N., Rupen, M.P., Dwarkadas, V.V., Beasley, A.J., Graham, D.A., Venturu, T., Umana, G., Cannon, W., Conway, J.: Radio Imaging of SN1993J: The Story Continues. In: 10th European VLBI Network Symposium and EVN Users Meeting: VLBI and the New Generation of Radio Arrays, p. 57 (2010)
12. Bietenholz, M.F., Bartel, N., Rupen, M.P.: SN 1993J VLBI. III. The Evolution of the Radio Shell. *ApJ* **597**, 374–398 (2003). DOI 10.1086/378265
13. Bietenholz, M.F., Bartel, N., Rupen, M.P.: Supernova 1986J Very Long Baseline Interferometry. II. The Evolution of the Shell and the Central Source. *ApJ* **712**, 1057–1069 (2010). DOI 10.1088/0004-637X/712/2/1057
14. Björnsson, C.I.: Inhomogeneities in Type Ib/c Supernovae: An Inverse Compton Scattering Origin of the X-Ray Emission. *ApJ* **769**, 65 (2013). DOI 10.1088/0004-637X/769/1/65
15. Björnsson, C.I., Fransson, C.: The X-Ray and Radio Emission from SN 2002ap: The Importance of Compton Scattering. *ApJ* **605**, 823–829 (2004). DOI 10.1086/382584
16. Björnsson, C.I., Lundqvist, P.: Heating from Free-Free Absorption and the Mass-loss Rate of the Progenitor Stars to Supernovae. *ApJ* **787**, 143 (2014). DOI 10.1088/0004-637X/787/2/143
17. Blondin, J.M., Lundqvist, P.: Formation of the circumstellar shell around SN 1987A. *ApJ* **405**, 337–352 (1993). DOI 10.1086/172366
18. Blondin, J.M., Lundqvist, P., Chevalier, R.A.: Axisymmetric Circumstellar Interaction in Supernovae. *ApJ* **472**, 257 (1996). DOI 10.1086/178060
19. Borkowski, K.J., Blondin, J.M., McCray, R.: X-Rays from the Impact of SN 1987A with its Circumstellar Ring. *ApJ* **477**, 281–293 (1997)
20. Burrows, C.J., Krist, J., Hester, J.J., Sahai, R., Trauger, J.T., Stapelfeldt, K.R., Gallagher III, J.S., Ballester, G.E., Casertano, S., Clarke, J.T., Crisp, D., Evans, R.W., Griffiths, R.E., Hoessel, J.G., Holtzman, J.A., Mould, J.R., Scowen, P.A., Watson, A.M., Westphal, J.A.: Hubble Space Telescope Observations of the SN 1987A Triple Ring Nebula. *ApJ* **452**, 680 (1995). DOI 10.1086/176339

21. Caprioli, D.: Cosmic-ray Acceleration and Propagation. ArXiv e-prints (2015)
22. Caprioli, D., Spitkovsky, A.: Simulations of Ion Acceleration at Non-relativistic Shocks. I. Acceleration Efficiency. *ApJ* **783**, 91 (2014). DOI 10.1088/0004-637X/783/2/91
23. Caprioli, D., Spitkovsky, A.: Simulations of Ion Acceleration at Non-relativistic Shocks. II. Magnetic Field Amplification. *ApJ* **794**, 46 (2014). DOI 10.1088/0004-637X/794/1/46
24. Caprioli, D., Spitkovsky, A.: Simulations of Ion Acceleration at Non-relativistic Shocks. III. Particle Diffusion. *ApJ* **794**, 47 (2014). DOI 10.1088/0004-637X/794/1/47
25. Chandra, P., Chevalier, R.A., Chugai, N., Fransson, C., Soderberg, A.M.: X-Ray and Radio Emission from Type II_n Supernova SN 2010jl. *ApJ* **810**, 32 (2015). DOI 10.1088/0004-637X/810/1/32
26. Chandra, P., Dwarkadas, V.V., Ray, A., Immler, S., Pooley, D.: X-rays from the Explosion Site: 15 Years of Light Curves of SN 1993J. *ApJ* **699**, 388–399 (2009). DOI 10.1088/0004-637X/699/1/388
27. Chevalier, R., Blondin, J.M.: Hydrodynamic instabilities in supernova remnants: Early radiative cooling. *ApJ* **444**, 312–317 (1995). DOI 10.1086/175606
28. Chevalier, R.A.: Self-similar solutions for the interaction of stellar ejecta with an external medium. *ApJ* **258**, 790–797 (1982). DOI 10.1086/160126
29. Chevalier, R.A.: The radio and X-ray emission from type II supernovae. *ApJ* **259**, 302–310 (1982). DOI 10.1086/160167
30. Chevalier, R.A.: The interaction of supernovae with a circumstellar medium. *Annals of the New York Academy of Sciences* **422**, 215–232 (1984). DOI 10.1111/j.1749-6632.1984.tb23355.x
31. Chevalier, R.A.: Interaction of supernovae with circumstellar matter. In: A.G. Petschek (ed.) *Supernovae*, pp. 91–110 (1990)
32. Chevalier, R.A.: Synchrotron Self-Absorption in Radio Supernovae. *ApJ* **499**, 810–819 (1998)
33. Chevalier, R.A.: Circumstellar Interaction around Supernovae. In: S. Immler, K. Weiler, R. McCray (eds.) *Supernova 1987A: 20 Years After: Supernovae and Gamma-Ray Bursters, American Institute of Physics Conference Series*, vol. 937, pp. 206–211 (2007). DOI 10.1063/1.3682904
34. Chevalier, R.A.: Common Envelope Evolution Leading to Supernovae with Dense Interaction. *ApJL* **752**, L2 (2012). DOI 10.1088/2041-8205/752/1/L2
35. Chevalier, R.A., Blondin, J.M., Emmering, R.T.: Hydrodynamic instabilities in supernova remnants - Self-similar driven waves. *ApJ* **392**, 118–130 (1992). DOI 10.1086/171411
36. Chevalier, R.A., Dwarkadas, V.V.: The Presupernova H II Region around SN 1987A. *ApJL* **452**, L45 (1995). DOI 10.1086/309714
37. Chevalier, R.A., Fransson, C.: Supernova interaction with a circumstellar wind and the distance to SN 1979c. In: N. Bartel (ed.) *Supernovae as Distance Indicators, Lecture Notes in Physics, Berlin Springer Verlag*, vol. 224 (1985)
38. Chevalier, R.A., Fransson, C.: Emission from circumstellar interaction in normal Type II supernovae. *ApJ* **420**, 268–285 (1994). DOI 10.1086/173557
39. Chevalier, R.A., Fransson, C.: Supernova Interaction with a Circumstellar Medium. In: K. Weiler (ed.) *Supernovae and Gamma-Ray Bursters, Lecture Notes in Physics, Berlin Springer Verlag*, vol. 598, pp. 171–194 (2003). DOI 10.1007/978-3-540-00123-0_123
40. Chevalier, R.A., Fransson, C.: Circumstellar Emission from Type Ib and Ic Supernovae. *ApJ* **651**, 381–391 (2006). DOI 10.1086/507606
41. Chevalier, R.A., Fransson, C., Nymark, T.K.: Radio and X-Ray Emission as Probes of Type IIP Supernovae and Red Supergiant Mass Loss. *ApJ* **641**, 1029–1038 (2006). DOI 10.1086/500528
42. Chevalier, R.A., Irwin, C.M.: X-Rays from Supernova Shocks in Dense Mass Loss. *ApJL* **747**, L17 (2012). DOI 10.1088/2041-8205/747/1/L17
43. Chevalier, R.A., Liang, E.P.: The interaction of supernovae with circumstellar bubbles. *ApJ* **344**, 332–340 (1989). DOI 10.1086/167802
44. Chevalier, R.A., Soker, N.: Asymmetric envelope expansion of supernova 1987A. *ApJ* **341**, 867–882 (1989). DOI 10.1086/167545

45. Chomiuk, L., Soderberg, A.M., Chevalier, R.A., Bruzewski, S., Foley, R.J., Parrent, J., Strader, J., Badenes, C., Fransson, C., Kamble, A., Margutti, R., Rupen, M.P., Simon, J.D.: A Deep Search for Prompt Radio Emission from Thermonuclear Supernovae with the Very Large Array. *ApJ* **821**, 119 (2016). DOI 10.3847/0004-637X/821/2/119
46. Chugai, N.N.: X-rays from SN 1986J - Emission of a shocked clumpy wind. *ApJL* **414**, L101–L103 (1993). DOI 10.1086/187006
47. Chugai, N.N.: Broad emission lines from the opaque electron-scattering environment of SN 1998S. *MNRAS* **326**, 1448–1454 (2001). DOI 10.1111/j.1365-2966.2001.04717.x
48. Chugai, N.N.: Circumstellar interaction in type Ibn supernovae and SN 2006jc. *MNRAS* **400**, 866–874 (2009). DOI 10.1111/j.1365-2966.2009.15506.x
49. Chugai, N.N., Belous, M.L.: Radio supernovae in a cloudy wind. *Astronomy Reports* **43**, 89–93 (1999)
50. Chugai, N.N., Chevalier, R.A.: Late Emission from the Type Ib/c SN 2001em: Overtaking the Hydrogen Envelope. *ApJ* **641**, 1051–1059 (2006). DOI 10.1086/500539
51. Chugai, N.N., Danziger, I.J.: Supernova 1988Z - Low-Mass Ejecta Colliding with the Clumpy Wind. *MNRAS* **268**, 173 (1994). DOI 10.1093/mnras/268.1.173
52. Chugai, N.N., Danziger, I.J., della Valle, M.: Optical spectrum of SN 1978K: emission from shocked clouds in the circumstellar wind. *MNRAS* **276**, 530–536 (1995). DOI 10.1093/mnras/276.2.530
53. Dessart, L., Audit, E., Hillier, D.J.: Numerical simulations of superluminous supernovae of type IIn. *MNRAS* **449**, 4304–4325 (2015). DOI 10.1093/mnras/stv609
54. Dewey, D., Zhekov, S.A., McCray, R., Canizares, C.R.: Chandra HETG Spectra of SN 1987A at 20 Years. *ApJL* **676**, L131 (2008). DOI 10.1086/587549
55. Drury, L.O.: An introduction to the theory of diffusive shock acceleration of energetic particles in tenuous plasmas. *Reports on Progress in Physics* **46**, 973–1027 (1983). DOI 10.1088/0034-4885/46/8/002
56. Dwarkadas, V.V.: On the lack of X-ray bright Type IIP supernovae. *MNRAS* **440**, 1917–1924 (2014). DOI 10.1093/mnras/stu347
57. Dwarkadas, V.V., Gruszko, J.: What are published X-ray light curves telling us about young supernova expansion? *MNRAS* **419**, 1515–1524 (2012). DOI 10.1111/j.1365-2966.2011.19808.x
58. Dwek, E.: The infrared diagnostic of a dusty plasma with applications to supernova remnants. *ApJ* **322**, 812–821 (1987). DOI 10.1086/165774
59. Ensman, L., Burrows, A.: Shock breakout in SN 1987A. *ApJ* **393**, 742–755 (1992). DOI 10.1086/171542
60. Fabian, A.C., Terlevich, R.: X-ray detection of Supernova 1988Z with the ROSAT High Resolution Imager. *MNRAS* **280**, L5–L8 (1996). DOI 10.1093/mnras/280.1.L5
61. Fassia, A., Meikle, W.P.S., Chugai, N., Geballe, T.R., Lundqvist, P., Walton, N.A., Pollacco, D., Veilleux, S., Wright, G.S., Pettini, M., Kerr, T., Puchnarewicz, E., Puxley, P., Irwin, M., Packham, C., Smartt, S.J., Harmer, D.: Optical and infrared spectroscopy of the type IIn SN 1998S: days 3–127. *MNRAS* **325**, 907–930 (2001). DOI 10.1046/j.1365-8711.2001.04282.x
62. Felten, J.E., Morrison, P.: Omnidirectional Inverse Compton and Synchrotron Radiation from Cosmic Distributions of Fast Electrons and Thermal Photons. *ApJ* **146**, 686 (1966). DOI 10.1086/148946
63. Filippenko, A.V., Barth, A.J., Matheson, T., Armus, L., Brown, M., Espey, B.R., Fan, X.M., Goodrich, R.W., Ho, L.C., Junkkarinen, V.T., Koo, D.C., Lehnert, M.D., Martel, A.R., Mazzarella, J.M., Miller, J.S., Smith, G.H., Tytler, D., Wirth, G.D.: The Type IC Supernova 1994I in M51: Detection of Helium and Spectral Evolution. *ApJL* **450**, L11 (1995). DOI 10.1086/309659
64. Foley, R.J., Smith, N., Ganeshalingam, M., Li, W., Chornock, R., Filippenko, A.V.: SN 2006jc: A Wolf-Rayet Star Exploding in a Dense He-rich Circumstellar Medium. *ApJL* **657**, L105–L108 (2007). DOI 10.1086/513145
65. Frank, K.A., Zhekov, S.A., Park, S., McCray, R., Dwek, E., Burrows, D.N.: Chandra Observes the End of an Era in SN 1987A. *ApJ* **829**, 40 (2016). DOI 10.3847/0004-637X/829/1/40

66. Fransson, C.: X-ray and UV-emission from supernova shock waves in stellar winds. *A&A* **111**, 140–150 (1982)
67. Fransson, C.: Comptonization and UV emission lines from Type II supernovae. *A&A* **133**, 264–284 (1984)
68. Fransson, C., Benvenuti, P., Wamsteker, W., Gordon, C., Hempe, K., Reimers, D., Palumbo, G.G.C., Panagia, N.: Physical conditions in the UV line emitting region of supernova 1979c in NGC 4321. *A&A* **132**, 1–10 (1984)
69. Fransson, C., Björnsson, C.I.: Radio Emission and Particle Acceleration in SN 1993J. *ApJ* **509**, 861–878 (1998). DOI 10.1086/306531
70. Fransson, C., Cassatella, A., Gilmozzi, R., Kirshner, R.P., Panagia, N., Sonneborn, G., Wamsteker, W.: Narrow ultraviolet emission lines from SN 1987A - Evidence for CNO processing in the progenitor. *ApJ* **336**, 429–441 (1989). DOI 10.1086/167022
71. Fransson, C., Challis, P.M., Chevalier, R.A., Filippenko, A.V., Kirshner, R.P., Kozma, C., Leonard, D.C., Matheson, T., Baron, E., Garnavich, P., Jha, S., Leibundgut, B., Lundqvist, P., Pun, C.S.J., Wang, L., Wheeler, J.C.: Hubble Space Telescope and Ground-based Observations of SN 1993J and SN 1998S: CNO Processing in the Progenitors. *ApJ* **622**, 991–1007 (2005). DOI 10.1086/426495
72. Fransson, C., Chevalier, R.A., Filippenko, A.V., Leibundgut, B., Barth, A.J., Fesen, R.A., Kirshner, R.P., Leonard, D.C., Li, W., Lundqvist, P., Sollerman, J., Van Dyk, S.D.: Optical and Ultraviolet Spectroscopy of SN 1995N: Evidence for Strong Circumstellar Interaction. *ApJ* **572**, 350–370 (2002). DOI 10.1086/340295
73. Fransson, C., Ergon, M., Challis, P.J., Chevalier, R.A., France, K., Kirshner, R.P., Marion, G.H., Milisavljevic, D., Smith, N., Bufano, F., Friedman, A.S., Kangas, T., Larsson, J., Mattila, S., Benetti, S., Chornock, R., Czekala, I., Soderberg, A., Sollerman, J.: High-density Circumstellar Interaction in the Luminous Type II In SN 2010jl: The First 1100 Days. *ApJ* **797**, 118 (2014). DOI 10.1088/0004-637X/797/2/118
74. Fransson, C., Larsson, J., Migotto, K., Pesce, D., Challis, P., Chevalier, R.A., France, K., Kirshner, R.P., Leibundgut, B., Lundqvist, P., McCray, R., Spyromilio, J., Taddia, F., Jerkstrand, A., Mattila, S., Smith, N., Sollerman, J., Wheeler, J.C., Crotts, A., Garnavich, P., Heng, K., Lawrence, S.S., Panagia, N., Pun, C.S.J., Sonneborn, G., Sugerman, B.: The Destruction of the Circumstellar Ring of SN 1987A. *ApJL* **806**, L19 (2015). DOI 10.1088/2041-8205/806/1/L19
75. Fransson, C., Larsson, J., Spyromilio, J., Chevalier, R., Gröningsson, P., Jerkstrand, A., Leibundgut, B., McCray, R., Challis, P., Kirshner, R.P., Kjaer, K., Lundqvist, P., Sollerman, J.: Late Spectral Evolution of the Ejecta and Reverse Shock in SN 1987A. *ApJ* **768**, 88 (2013). DOI 10.1088/0004-637X/768/1/88
76. Fransson, C., Lundqvist, P., Chevalier, R.A.: Circumstellar Interaction in SN 1993J. *ApJ* **461**, 993 (1996). DOI 10.1086/177119
77. Gröningsson, P., Fransson, C., Lundqvist, P., Lundqvist, N., Leibundgut, B., Spyromilio, J., Chevalier, R.A., Gilmozzi, R., Kjær, K., Mattila, S., Sollerman, J.: High resolution spectroscopy of the inner ring of SN 1987A. *A&A* **479**, 761–777 (2008). DOI 10.1051/0004-6361:20077604
78. Gröningsson, P., Fransson, C., Lundqvist, P., Lundqvist, N., Leibundgut, B., Spyromilio, J., Chevalier, R.A., Gilmozzi, R., Kjær, K., Mattila, S., Sollerman, J.: High resolution spectroscopy of the inner ring of SN 1987A. *A&A* **479**, 761–777 (2008). DOI 10.1051/0004-6361:20077604
79. Gröningsson, P., Fransson, C., Lundqvist, P., Nymark, T., Lundqvist, N., Chevalier, R., Leibundgut, B., Spyromilio, J.: Coronal emission from the shocked circumstellar ring of SN 1987A. *A&A* **456**, 581–589 (2006). DOI 10.1051/0004-6361:20065325
80. Haberl, F., Geppert, U., Aschenbach, B., Hasinger, G.: XMM-Newton observations of μ AS-TROBJ₂SN 1987 A₁/ASTROBJ₂. *A&A* **460**, 811–819 (2006). DOI 10.1051/0004-6361:20066198
81. Horesh, A., Kulkarni, S.R., Fox, D.B., Carpenter, J., Kasliwal, M.M., Ofek, E.O., Quimby, R., Gal-Yam, A., Cenko, S.B., de Bruyn, A.G., Kamble, A., Wijers, R.A.M.J., van der Horst,

- A.J., Kouveliotou, C., Podsiadlowski, P., Sullivan, M., Maguire, K., Howell, D.A., Nugent, P.E., Gehrels, N., Law, N.M., Poznanski, D., Shara, M.: Early Radio and X-Ray Observations of the Youngest nearby Type Ia Supernova PTF 11kly (SN 2011fe). *ApJ* **746**, 21 (2012). DOI 10.1088/0004-637X/746/1/21
82. Houck, J.C., Bregman, J.N., Chevalier, R.A., Tomisaka, K.: Recent X-Ray Observations of SN 1986J with ASCA and ROSAT. *ApJ* **493**, 431–439 (1998). DOI 10.1086/305098
83. Immler, S., Modjaz, M., Landsman, W., Bufano, F., Brown, P.J., Milne, P., Dessart, L., Holland, S.T., Koss, M., Pooley, D., Kirshner, R.P., Filippenko, A.V., Panagia, N., Chevalier, R.A., Mazzali, P.A., Gehrels, N., Petre, R., Burrows, D.N., Nousek, J.A., Roming, P.W.A., Pian, E., Soderberg, A.M., Greiner, J.: Swift and Chandra Detections of Supernova 2006jc: Evidence for Interaction of the Supernova Shock with a Circumstellar Shell. *ApJL* **674**, L85 (2008). DOI 10.1086/529373
84. Immler, S., Wilson, A.S., Terashima, Y.: X-Ray Emission from the Type Ic Supernova 1994I Observed with Chandra. *ApJL* **573**, L27–L30 (2002). DOI 10.1086/341935
85. Jakobsen, P., Albrecht, R., Barbieri, C., Blades, J.C., Boksenberg, A., Crane, P., Deharveng, J.M., Disney, M.J., Kamperman, T.M., King, I.R., Macchetto, F., Mackay, C.D., Paresce, F., Weigelt, G., Baxter, D., Greenfield, P., Jedrzejewski, R., Nota, A., Sparks, W.B., Kirshner, R.P., Panagia, N.: First results from the Faint Object Camera - SN 1987A. *ApJL* **369**, L66–L66 (1991). DOI 10.1086/185959
86. Jones, F.C., Ellison, D.C.: The plasma physics of shock acceleration. *SSRv* **58**, 259–346 (1991). DOI 10.1007/BF01206003
87. Jun, B.I., Jones, T.W., Norman, M.L.: Interaction of Rayleigh-Taylor Fingers and Circumstellar Cloudlets in Young Supernova Remnants. *ApJL* **468**, L59 (1996). DOI 10.1086/310224
88. Kallman, T.R., McCray, R.: X-ray nebular models. *ApJS* **50**, 263–317 (1982). DOI 10.1086/190828
89. Kuncarayakti, H., Maeda, K., Anderson, J.P., Hamuy, M., Nomoto, K., Galbany, L., Doi, M.: Evolving into a remnant: optical observations of SN 1978K at three decades. *MNRAS* **458**, 2063–2073 (2016). DOI 10.1093/mnras/stw430
90. Larsson, J., Fransson, C., Östlin, G., Gröningsson, P., Jerkstrand, A., Kozma, C., Sollerman, J., Challis, P., Kirshner, R.P., Chevalier, R.A., Heng, K., McCray, R., Suntzeff, N.B., Bouchet, P., Crotts, A., Danziger, J., Dwek, E., France, K., Garnavich, P.M., Lawrence, S.S., Leibundgut, B., Lundqvist, P., Panagia, N., Pun, C.S.J., Smith, N., Sonneborn, G., Wang, L., Wheeler, J.C.: X-ray illumination of the ejecta of supernova 1987A. *Nature* **474**, 484–486 (2011). DOI 10.1038/nature10090
91. Leising, M.D., Kurfess, J.D., Clayton, D.D., Grabelsky, D.A., Grove, J.E., Johnson, W.N., Jung, G.V., Kinzer, R.L., Kroeger, R.A., Purcell, W.R., Strickman, M.S., The, L.S., Ulmer, M.P.: Hard X-rays from SN 1993J. *ApJL* **431**, L95–L98 (1994). DOI 10.1086/187481
92. Longair, M.S.: *High Energy Astrophysics* (2011)
93. Lundqvist, P., Fransson, C.: Circumstellar absorption of UV and radio emission from supernovae. *A&A* **192**, 221–233 (1988)
94. Lundqvist, P., Fransson, C.: The Line Emission from the Circumstellar Gas around SN 1987A. *ApJ* **464**, 924 (1996). DOI 10.1086/177380
95. Marcaide, J.M., Martí-Vidal, I., Alberdi, A., Pérez-Torres, M.A., Ros, E., Diamond, P.J., Guirado, J.C., Lara, L., Shapiro, I.I., Stockdale, C.J., Weiler, K.W., Mantovani, F., Preston, R.A., Schilizzi, R.T., Sramek, R.A., Trigilio, C., van Dyk, S.D., Whitney, A.R.: A decade of SN 1993J: discovery of radio wavelength effects in the expansion rate. *A&A* **505**, 927–945 (2009). DOI 10.1051/0004-6361/200912133
96. Marcaide, J.M., Martí-Vidal, I., Pérez-Torres, M.A., Alberdi, A., Guirado, J.C., Ros, E., Weiler, K.W.: 1.6 GHz VLBI observations of SN 1979C: almost-free expansion. *A&A* **503**, 869–872 (2009). DOI 10.1051/0004-6361/200912485
97. Marcowith, A., Bret, A., Bykov, A., Dieckman, M.E., O’C Drury, L., Lembège, B., Lemoine, M., Morlino, G., Murphy, G., Pelletier, G., Plotnikov, I., Reville, B., Riquelme, M., Sironi, L., Stockem Novo, A.: The microphysics of collisionless shock waves. *Reports on Progress in Physics* **79**(4), 046901 (2016). DOI 10.1088/0034-4885/79/4/046901

98. Margutti, R., Kamble, A., Milisavljevic, D., De Mink, S., Zapartas, E., Drout, M., Chornock, R., Risaliti, G., Zauderer, B.A., Bietenholz, M., Cantiello, M., Chakraborti, S., Chomiuk, L., Fong, W., Grefenstette, B., Guidorzi, C., Kirshner, R., Parrent, J.T., Patnaude, D., Soderberg, A.M., Gehrels, N.C., Harrison, F.: Ejection of the massive Hydrogen-rich envelope timed with the collapse of the stripped SN2014C. ArXiv e-prints (2016)
99. Margutti, R., Parrent, J., Kamble, A., Soderberg, A.M., Foley, R.J., Milisavljevic, D., Drout, M.R., Kirshner, R.: No X-Rays from the Very Nearby Type Ia SN 2014J: Constraints on Its Environment. *ApJ* **790**, 52 (2014). DOI 10.1088/0004-637X/790/1/52
100. Martí-Vidal, I., Marcaide, J.M., Alberdi, A., Guirado, J.C., Lara, L., Pérez-Torres, M.A., Ros, E., Argo, M.K., Beswick, R.J., Muxlow, T.W.B., Pedlar, A., Shapiro, I.I., Stockdale, C.J., Sramek, R.A., Weiler, K.W., Vinko, J.: 8.4 GHz VLBI observations of SN 2004et in NGC 6946. *A&A* **470**, 1071–1077 (2007). DOI 10.1051/0004-6361:20077522
101. Martí-Vidal, I., Marcaide, J.M., Alberdi, A., Guirado, J.C., Pérez-Torres, M.A., Ros, E.: Radio emission of SN1993J: the complete picture. II. Simultaneous fit of expansion and radio light curves. *A&A* **526**, A143 (2011). DOI 10.1051/0004-6361/201014517
102. Matheson, T., Filippenko, A.V., Barth, A.J., Ho, L.C., Leonard, D.C., Bershad, M.A., Davis, M., Finley, D.S., Fisher, D., González, R.A., Hawley, S.L., Koo, D.C., Li, W., Lonsdale, C.J., Schlegel, D., Smith, H.E., Spinrad, H., Wirth, G.D.: Optical Spectroscopy of Supernova 1993J During Its First 2500 Days. *AJ* **120**, 1487–1498 (2000). DOI 10.1086/301518
103. Matheson, T., Filippenko, A.V., Barth, A.J., Ho, L.C., Leonard, D.C., Bershad, M.A., Davis, M., Finley, D.S., Fisher, D., González, R.A., Hawley, S.L., Koo, D.C., Li, W., Lonsdale, C.J., Schlegel, D., Smith, H.E., Spinrad, H., Wirth, G.D.: Optical Spectroscopy of Supernova 1993J During Its First 2500 Days. *AJ* **120**, 1487–1498 (2000). DOI 10.1086/301518
104. Matheson, T., Filippenko, A.V., Ho, L.C., Barth, A.J., Leonard, D.C.: Detailed Analysis of Early to Late-Time Spectra of Supernova 1993J. *AJ* **120**, 1499–1515 (2000). DOI 10.1086/301519
105. Mattila, S., Meikle, W.P.S., Lundqvist, P., Pastorello, A., Kotak, R., Eldridge, J., Smartt, S., Adamson, A., Gerardy, C.L., Rizzi, L., Stephens, A.W., van Dyk, S.D.: Massive stars exploding in a He-rich circumstellar medium - III. SN 2006jc: infrared echoes from new and old dust in the progenitor CSM. *MNRAS* **389**, 141–155 (2008). DOI 10.1111/j.1365-2966.2008.13516.x
106. Matzner, C.D., McKee, C.F.: The Expulsion of Stellar Envelopes in Core-Collapse Supernovae. *ApJ* **510**, 379–403 (1999). DOI 10.1086/306571
107. McCray, R., Fransson, C.: The Remnant of Supernova 1987A. *ARA&A* **16** (2016). DOI 10.1146/annurev-astro-082615-105405
108. McDonald, A.R., Muxlow, T.W.B., Pedlar, A., Garrett, M.A., Wills, K.A., Garrington, S.T., Diamond, P.J., Wilkinson, P.N.: Global very long-baseline interferometry observations of compact radio sources in M82. *MNRAS* **322**, 100–106 (2001). DOI 10.1046/j.1365-8711.2001.04109.x
109. Milisavljevic, D., Fesen, R.A., Chevalier, R.A., Kirshner, R.P., Challis, P., Turatto, M.: Late-time Optical Emission from Core-collapse Supernovae. *ApJ* **751**, 25 (2012). DOI 10.1088/0004-637X/751/1/25
110. Milisavljevic, D., Fesen, R.A., Leibundgut, B., Kirshner, R.P.: The Evolution of Late-Time Optical Emission from SN 1986J. *ApJ* **684**, 1170–1173 (2008). DOI 10.1086/590426
111. Milisavljevic, D., Margutti, R., Kamble, A., Patnaude, D.J., Raymond, J.C., Eldridge, J.J., Fong, W., Bietenholz, M., Challis, P., Chornock, R., Drout, M.R., Fransson, C., Fesen, R.A., Grindlay, J.E., Kirshner, R.P., Lunnan, R., Mackey, J., Miller, G.F., Parent, J.T., Sanders, N.E., Soderberg, A.M., Zauderer, B.A.: Metamorphosis of SN 2014C: Delayed Interaction between a Hydrogen Poor Core-collapse Supernova and a Nearby Circumstellar Shell. *ApJ* **815**, 120 (2015). DOI 10.1088/0004-637X/815/2/120
112. Murase, K., Thompson, T.A., Lacki, B.C., Beacom, J.F.: New class of high-energy transients from crashes of supernova ejecta with massive circumstellar material shells. *PhRvD* **84**(4), 043003 (2011). DOI 10.1103/PhysRevD.84.043003

113. Murase, K., Thompson, T.A., Ofek, E.O.: Probing cosmic ray ion acceleration with radio-submm and gamma-ray emission from interaction-powered supernovae. *MNRAS* **440**, 2528–2543 (2014). DOI 10.1093/mnras/stu384
114. Nadezhin, D.K.: On the initial phase of interaction between expanding stellar envelopes and surrounding medium. *Ap&SS* **112**, 225–249 (1985). DOI 10.1007/BF00653506
115. Nakar, E.: A Unified Picture for Low-luminosity and Long Gamma-Ray Bursts Based on the Extended Progenitor of IIGRB 060218/SN 2006aj. *ApJ* **807**, 172 (2015). DOI 10.1088/0004-637X/807/2/172
116. Nakar, E., Sari, R.: Relativistic Shock Breakouts – A Variety of Gamma-Ray Flares: From Low-luminosity Gamma-Ray Bursts to Type Ia Supernovae. *ApJ* **747**, 88 (2012). DOI 10.1088/0004-637X/747/2/88
117. Ng, C.Y., Zanardo, G., Potter, T.M., Staveley-Smith, L., Gaensler, B.M., Manchester, R.N., Tzioumis, A.K.: Evolution of the Radio Remnant of Supernova 1987A: Morphological Changes from Day 7000. *ApJ* **777**, 131 (2013). DOI 10.1088/0004-637X/777/2/131
118. Nomoto, K., Suzuki, T.: X-Rays from Supernova 1993J; Ejecta Instabilities. In: K. Koyama, S. Kitamoto, M. Itoh (eds.) *The Hot Universe, IAU Symposium*, vol. 188, p. 27 (1998)
119. Nymark, T.K., Chandra, P., Fransson, C.: Modeling the X-ray emission of SN 1993J. *A&A* **494**, 179–189 (2009). DOI 10.1051/0004-6361:200810884
120. Nymark, T.K., Fransson, C., Kozma, C.: X-ray emission from radiative shocks in type II supernovae. *A&A* **449**, 171–192 (2006). DOI 10.1051/0004-6361:20054169
121. Ofek, E.O., Fox, D., Cenko, S.B., Sullivan, M., Gnat, O., Frail, D.A., Horesh, A., Corsi, A., Quimby, R.M., Gehrels, N., Kulkarni, S.R., Gal-Yam, A., Nugent, P.E., Yaron, O., Filippenko, A.V., Kasliwal, M.M., Bildsten, L., Bloom, J.S., Poznanski, D., Arcavi, I., Laher, R.R., Levitan, D., Sesar, B., Surace, J.: X-Ray Emission from Supernovae in Dense Circumstellar Matter Environments: A Search for Collisionless Shocks. *ApJ* **763**, 42 (2013). DOI 10.1088/0004-637X/763/1/42
122. Ofek, E.O., Zoglauer, A., Boggs, S.E., Barrière, N.M., Reynolds, S.P., Fryer, C.L., Harrison, F.A., Cenko, S.B., Kulkarni, S.R., Gal-Yam, A., Arcavi, I., Bellm, E., Bloom, J.S., Christensen, F., Craig, W.W., Even, W., Filippenko, A.V., Grefenstette, B., Hailey, C.J., Laher, R., Madsen, K., Nakar, E., Nugent, P.E., Stern, D., Sullivan, M., Surace, J., Zhang, W.W.: SN 2010jl: Optical to Hard X-Ray Observations Reveal an Explosion Embedded in a Ten Solar Mass Cocoon. *ApJ* **781**, 42 (2014). DOI 10.1088/0004-637X/781/1/42
123. Orlando, S., Miceli, M., Pumo, M.L., Bocchino, F.: Supernova 1987A: a Template to Link Supernovae to Their Remnants. *ApJ* **810**, 168 (2015). DOI 10.1088/0004-637X/810/2/168
124. Pacholczyk, A.G.: Radio astrophysics. Nonthermal processes in galactic and extragalactic sources (1970)
125. Park, J., Caprioli, D., Spitkovsky, A.: Simultaneous Acceleration of Protons and Electrons at Nonrelativistic Quasiparallel Collisionless Shocks. *Physical Review Letters* **114**(8), 085003 (2015). DOI 10.1103/PhysRevLett.114.085003
126. Pastorello, A., Smartt, S.J., Mattila, S., Eldridge, J.J., Young, D., Itagaki, K., Yamaoka, H., Navasardyan, H., Valenti, S., Patat, F., Agnoletto, I., Augusteijn, T., Benetti, S., Cappellaro, E., Boles, T., Bonnet-Bidaud, J.M., Botticella, M.T., Bufano, F., Cao, C., Deng, J., Dennefeld, M., Elias-Rosa, N., Harutyunyan, A., Keenan, F.P., Iijima, T., Lorenzi, V., Mazzali, P.A., Meng, X., Nakano, S., Nielsen, T.B., Smoker, J.V., Stanishev, V., Turatto, M., Xu, D., Zampieri, L.: A giant outburst two years before the core-collapse of a massive star. *Nature* **447**, 829–832 (2007). DOI 10.1038/nature05825
127. Pastorello, A., Wang, X.F., Ciabattari, F., Bersier, D., Mazzali, P.A., Gao, X., Xu, Z., Zhang, J.J., Tokuoka, S., Benetti, S., Cappellaro, E., Elias-Rosa, N., Harutyunyan, A., Huang, F., Miluzio, M., Mo, J., Ochner, P., Tartaglia, L., Terreran, G., Tomasella, L., Turatto, M.: Massive stars exploding in a He-rich circumstellar medium - IX. SN 2014av, and characterization of Type Ib SNe. *MNRAS* **456**, 853–869 (2016). DOI 10.1093/mnras/stv2634
128. Pérez-Torres, M.A., Alberdi, A., Marcaide, J.M., Guirado, J.C., Lara, L., Mantovani, F., Ros, E., Weiler, K.W.: A distorted radio shell in the young supernova SN 1986J. *MNRAS* **335**, L23–L28 (2002). DOI 10.1046/j.1365-8711.2002.05809.x

129. Pérez-Torres, M.A., Lundqvist, P., Beswick, R.J., Björnsson, C.I., Muxlow, T.W.B., Paragi, Z., Ryder, S., Alberdi, A., Fransson, C., Marcaide, J.M., Martí-Vidal, I., Ros, E., Argo, M.K., Guirado, J.C.: Constraints on the Progenitor System and the Environs of SN 2014J from Deep Radio Observations. *ApJ* **792**, 38 (2014). DOI 10.1088/0004-637X/792/1/38
130. Potter, T.M., Staveley-Smith, L., Reville, B., Ng, C.Y., Bicknell, G.V., Sutherland, R.S., Wagner, A.Y.: Multi-dimensional Simulations of the Expanding Supernova Remnant of SN 1987A. *ApJ* **794**, 174 (2014). DOI 10.1088/0004-637X/794/2/174
131. Pozzo, M., Meikle, W.P.S., Fassia, A., Geballe, T., Lundqvist, P., Chugai, N.N., Sollerman, J.: On the source of the late-time infrared luminosity of SN 1998S and other Type II supernovae. *MNRAS* **352**, 457–477 (2004). DOI 10.1111/j.1365-2966.2004.07951.x
132. Rybicki, G.B., Lightman, A.P.: *Radiative Processes in Astrophysics* (1986)
133. Sakurai, A.: On the problem of a shock wave arriving at the edge of a gas. *Comm. Pure Appl. Math.* **13**, 353–370 (1960)
134. Shiode, J.H., Quataert, E.: Setting the Stage for Circumstellar Interaction in Core-Collapse Supernovae. II. Wave-driven Mass Loss in Supernova Progenitors. *ApJ* **780**, 96 (2014). DOI 10.1088/0004-637X/780/1/96
135. Slysh, V.I.: Synchrotron Self-Absorption of Radio Emission from Supernovae. *Soviet Astronomy Letters* **16**, 339 (1990)
136. Smith, N.: The Structure of the Homunculus. I. Shape and Latitude Dependence from H₂ and [Fe II] Velocity Maps of η Carinae. *ApJ* **644**, 1151–1163 (2006). DOI 10.1086/503766
137. Smith, N.: Mass Loss: Its Effect on the Evolution and Fate of High-Mass Stars. *ARA&A* **52**, 487–528 (2014). DOI 10.1146/annurev-astro-081913-040025
138. Smith, N., Arnett, W.D.: Preparing for an Explosion: Hydrodynamic Instabilities and Turbulence in Presupernovae. *ApJ* **785**, 82 (2014). DOI 10.1088/0004-637X/785/2/82
139. Smith, N., Foley, R.J., Filippenko, A.V.: Dust Formation and He II λ 4686 Emission in the Dense Shell of the Peculiar Type Ib Supernova 2006jc. *ApJ* **680**, 568–579 (2008). DOI 10.1086/587860
140. Smith, N., Hinkle, K.H., Ryde, N.: Red Supergiants as Potential Type II_n Supernova Progenitors: Spatially Resolved 4.6 μ m CO Emission Around VY CMa and Betelgeuse. *AJ* **137**, 3558–3573 (2009). DOI 10.1088/0004-6256/137/3/3558
141. Sramek, R.A., Weiler, K.W.: Radio Supernovae. In: K. Weiler (ed.) *Supernovae and Gamma-Ray Bursters, Lecture Notes in Physics, Berlin Springer Verlag*, vol. 598, pp. 145–169 (2003). DOI 123
142. Storey, M.C., Manchester, R.N.: Modelling of the radio burst from SN 1987A. *Nature* **329**, 421–423 (1987). DOI 10.1038/329421a0
143. Stritzinger, M., Taddia, F., Fransson, C., Fox, O.D., Morrell, N., Phillips, M.M., Sollerman, J., Anderson, J.P., Boldt, L., Brown, P.J., Campillay, A., Castellon, S., Contreras, C., Folatelli, G., Habergam, S.M., Hamuy, M., Hjorth, J., James, P.A., Krzeminski, W., Mattila, S., Persson, S.E., Roth, M.: Multi-wavelength Observations of the Enduring Type II_n Supernovae 2005ip and 2006jd. *ApJ* **756**, 173 (2012). DOI 10.1088/0004-637X/756/2/173
144. Taddia, F., Sollerman, J., Fremling, C., Pastorello, A., Leloudas, G., Fransson, C., Nyholm, A., Stritzinger, M.D., Ergon, M., Roy, R., Migotto, K.: Metallicity at the explosion sites of interacting transients. *A&A* **580**, A131 (2015). DOI 10.1051/0004-6361/201525989
145. Van Dyk, S.D., de Mink, S.E., Zapartas, E.: Constraints on the Binary Companion to the SN Ic 1994I Progenitor. *ApJ* **818**, 75 (2016). DOI 10.3847/0004-637X/818/1/75
146. van Dyk, S.D., Weiler, K.W., Sramek, R.A., Rupen, M.P., Panagia, N.: SN 1993J: The early radio emission and evidence for a changing presupernova mass-loss rate. *ApJL* **432**, L115–L118 (1994). DOI 10.1086/187525
147. van Marle, A.J., Smith, N., Owocki, S.P., van Veelen, B.: Numerical models of collisions between core-collapse supernovae and circumstellar shells. *MNRAS* **407**, 2305–2327 (2010). DOI 10.1111/j.1365-2966.2010.16851.x
148. Weiler, K.W., Panagia, N., Stockdale, C., Rupen, M., Sramek, R.A., Williams, C.L.: Radio Emission from SN 1994I in NGC 5194 (M 51): The Best-studied Type Ib/c Radio Supernova. *ApJ* **740**, 79 (2011). DOI 10.1088/0004-637X/740/2/79

149. Weiler, K.W., Sramek, R.A., Panagia, N., van der Hulst, J.M., Salvati, M.: Radio supernovae. *ApJ* **301**, 790–812 (1986). DOI 10.1086/163944
150. Weiler, K.W., van der Hulst, J.M., Sramek, R.A., Panagia, N.: SN 1979c - A radio supernova. *ApJL* **243**, L151–L156 (1981). DOI 10.1086/183463
151. Weiler, K.W., van Dyk, S.D., Pringle, J.E., Panagia, N.: Evidence for periodic modulation of presupernova mass loss from the progenitor of SN 1979 C. *ApJ* **399**, 672–679 (1992). DOI 10.1086/171959
152. Weiler, K.W., Williams, C.L., Panagia, N., Stockdale, C.J., Kelley, M.T., Sramek, R.A., Van Dyk, S.D., Marcaide, J.M.: Long-Term Radio Monitoring of SN 1993J. *ApJ* **671**, 1959–1980 (2007). DOI 10.1086/523258
153. Wellons, S., Soderberg, A.M., Chevalier, R.A.: Radio Observations Reveal Unusual Circumstellar Environments for Some Type Ibc Supernova Progenitors. *ApJ* **752**, 17 (2012). DOI 10.1088/0004-637X/752/1/17
154. Williams, C.L., Panagia, N., Van Dyk, S.D., Lacey, C.K., Weiler, K.W., Sramek, R.A.: Radio Emission from SN 1988Z and Very Massive Star Evolution. *ApJ* **581**, 396–403 (2002). DOI 10.1086/344087
155. Zandarò, G., Staveley-Smith, L., Ball, L., Gaensler, B.M., Kesteven, M.J., Manchester, R.N., Ng, C.Y., Tzioumis, A.K., Potter, T.M.: Multifrequency Radio Measurements of Supernova 1987A Over 22 Years. *ApJ* **710**, 1515–1529 (2010). DOI 10.1088/0004-637X/710/2/1515
156. Zhang, T., Wang, X., Wu, C., Chen, J., Chen, J., Liu, Q., Huang, F., Liang, J., Zhao, X., Lin, L., Wang, M., Dennefeld, M., Zhang, J., Zhai, M., Wu, H., Fan, Z., Zou, H., Zhou, X., Ma, J.: Type II In Supernova SN 2010jl: Optical Observations for over 500 Days after Explosion. *AJ* **144**, 131 (2012). DOI 10.1088/0004-6256/144/5/131
157. Zimmermann, H.U., Aschenbach, B.: XMM-Newton observation of SN 1993J in M 81. *A&A* **406**, 969–974 (2003). DOI 10.1051/0004-6361:20030687